



# Elucidating effects of catalyst loadings and porous transport layer morphologies on operation of proton exchange membrane water electrolyzers

Devashish Kulkarni<sup>a</sup>, Alex Huynh<sup>b,c</sup>, Pongsarun Satjaritanun<sup>b,c</sup>, Maeve O'Brien<sup>a</sup>, Sirivatch Shimpalee<sup>d</sup>, Dilworth Parkinson<sup>e</sup>, Pavel Shevchenko<sup>f</sup>, Francesco DeCarlo<sup>f</sup>, Nemanja Danilovic<sup>e</sup>, Katherine E. Ayers<sup>g</sup>, Christopher Capuano<sup>g</sup>, Iryna V. Zenyuk<sup>a,b,c,\*</sup>

<sup>a</sup> Department of Material Science and Engineering, University of California Irvine, Irvine, CA, USA

<sup>b</sup> National Fuel Cell Research Center, University of California Irvine, Irvine, CA, USA

<sup>c</sup> Department of Chemical and Biomolecular Engineering, University of California Irvine, Irvine, CA, USA

<sup>d</sup> Department of Chemical Engineering, University of South Carolina, Columbia, SC, USA

<sup>e</sup> Energy Technologies Area, Energy Conversion Group, Lawrence Berkeley National Laboratory, Berkeley, CA 94720, USA

<sup>f</sup> X-ray Science Division, Argonne National Laboratory, 9700S. Class Avenue, Lemont, IL, USA

<sup>g</sup> Nel Hydrogen, Wallingford, CT, USA

## ARTICLE INFO

### Keywords:

Proton exchange membrane water electrolysis  
X-ray computed tomography  
Catalyst layers  
Triple phase contact area  
Lattice Boltzmann method modeling  
Durability analysis

## ABSTRACT

Producing green hydrogen efficiently via proton exchange membrane water electrolysis (PEMWE) is the key for achieving decarbonization targets. Iridium catalyst is expensive, and it is important to minimize its use and to optimize interface between Ir and ionomer or water for higher utilization of catalyst in oxygen evolution reaction. In this paper, x-ray computed tomography along with electrochemical and modeling techniques are used to characterize the interface for two different porous transport layers (PTLs) and catalyst layers at various loadings. We show that low porosity sintered PTLs exhibit higher interfacial contact with the catalyst and the membrane that results in improved kinetics. Radiography and modeling results indicate that oxygen taking multiple transport pathways through the PTL results in slug flow through the channels that reduces mass transport overpotential. Based on the results, we suggest design guidelines for high efficiency and durable PEMWE and their components.

## 1. Introduction

As the world transitions to renewable power generation, such as wind and solar to decarbonize the energy sector, energy storage becomes critical to accommodate intermittency of renewables [1,2]. For short-duration energy storage (<10 h) battery technologies are well fit. For multi-day and long-duration or seasonal storage alternative energy storage technologies are needed. Fuels and chemicals can store electric energy for long duration with minimal self-discharge. However, infrastructure is needed to enable energy storage into chemicals. Using existing natural gas infrastructure, hydrogen economy is possible, as hydrogen can be stored in natural gas pipelines, in underground caverns and transported in liquified or compressed form [3–5]. Producing and storing green hydrogen from the excess curtailed renewable energy by

electrochemically splitting water is the cornerstone of the hydrogen economy [4,6,7]. Proton exchange membrane water electrolysis (PEMWE) is a promising technology that is gaining widespread popularity among the available electrolysis chemistries, due to its low temperature operation, low footprint, dynamic start up and response times, differential pressure operation and the ease of scalability [8,9]. Many countries are envisioning hydrogen-based economies, with the U.S. Department of Energy announcing \$64 million to support its H2@Scale initiative [10] in 2020 alone. The European Clean Hydrogen Alliance was launched by the European Union in 2020 and estimates investments of \$503 billion until 2030 [11]. Hydrogen production is targeted at a cost of \$2 per kg<sub>H2</sub> [12] in order to be competitive with steam water reforming (SMR) that uses traditional fossil fuels.

The electrochemical splitting of water by PEMWE involves the fast

\* Corresponding author at: Department of Chemical and Biomolecular Engineering, University of California Irvine, Irvine, CA, USA.

E-mail address: [Iryna.zenyuk@uci.edu](mailto:Iryna.zenyuk@uci.edu) (I.V. Zenyuk).

<https://doi.org/10.1016/j.apcatb.2022.121213>

Received 12 August 2021; Received in revised form 9 February 2022; Accepted 11 February 2022

Available online 15 February 2022

0926-3373/© 2022 Elsevier B.V. All rights reserved.

hydrogen evolution reaction (HER) on the cathode and the sluggish oxygen evolution reaction (OER) on the anode, as shown by Fig. 1a. The HER is facilitated by Pt-based electrocatalyst, whereas the OER is facilitated by the IrOx based electrocatalysts [13,14]. In acidic media, and under high applied potentials for anode, IrOx is one of the very few catalysts that is active and stable towards the OER. The use of these rare metals is a substantial cost driver specifically when MW scale deployment of PEMWE is envisioned to make the produced hydrogen cost competitive [15]. The availability of Ir is a growing concern since it is one of the rarest elements found in the earth's crust, mostly through meteorites with an estimated production of only  $\sim 7.25$  tons annually [16]. To enable wide-adoption of PEMWE to achieve 100% decarbonization of the energy sector, it is imperative to reduce catalyst loadings and improve the Ir-specific power of PEMWE, which is a measure of the potentiality of the catalyst. Current commercially available PEMWE systems have an Ir-specific power of  $\sim 2$  MW/kg<sub>Ir</sub> [17], when the current density is measured at a higher heating value (HHV) based efficiency of 88% (corresponds to Ir loading of 2–3 mg cm<sup>-2</sup>). However, this translates to a deployment of only 7.2 GW per year even if 50% of the annual production of Ir were to be used for PEMWE. Considering the combined energy required by the transportation sector, natural gas and electricity storage and assuming that this demand would be supplied by H<sub>2</sub>, a  $\sim 50$ -fold increase in the Ir-specific power to 100 MW/kg<sub>Ir</sub> [18] (corresponds to Ir loadings  $<0.01$  mg cm<sup>-2</sup> operated at commercial current densities) is needed.

The Ir-specific power density can be increased by either decreasing the Ir loading or increasing the operating current density and these strategies have been widely explored in literature [19–21]. Taie et al. [16] in their recent work investigated ultra-low loaded anodes up to 0.0035 mg cm<sup>-2</sup> for PEMWE considering the available Ir resources and the target of complete decarbonization of the energy sector by 2050. Developing stable and uniform catalyst layers at such low loadings requires significant effort, advanced manufacturing techniques, such as ultrasonic spray coating and optimization strategies. Moreover, extremely low catalyst loadings pose significant durability challenges and the maximum current density achieved may be insufficient for practical applications. Other ways to reduce Ir loadings are to create even dispersions of Ir on high surface area materials or thin films, such as TiC [21], TiO<sub>2</sub> [22] or nano structured thin films (NSTF) [23]. Usage of non-PGMs [24] and advanced core shell catalysts [15] for OER are also being studied to reduce or eliminate the technology's dependence on noble metals. However, these material development strategies are still at

the experimental stage and need more technical maturity to be commercialized. While these technical strides are important for reducing the future capital cost (CAPEX), the need of the hour is to minimize the operating costs (OPEX) of PEMWE by investigating the kinetic and mass transport losses [25] that are the major contributors to the cell overpotential and improving the durability of the existing systems. According to a recent analysis of PEMWE systems [26], the catalyst loading should be reduced as much as possible, while retaining the system performance and durability. Hence, optimizing performance of electrodes with catalyst loadings showing reasonable durability is the need of the hour.

Currently, there are limited studies dedicated to understanding the complex two-phase transport phenomenon through the anodic porous transport layer (PTL) and its effect on the PEMWE performance [27–30]. While it has been well established that the understanding and improving interfaces between the catalyst layer and the PTL is the key to improving PEMWE performance [31], the underlying processes that limit and affect catalyst utilization are still ambiguous. Several studies used neutron imaging to study the oxygen flow in the PEMWE channels [32–34] but neutron imaging is limited by spatial and temporal resolution. Leonard et al. [30] used x-ray computed tomography (CT) to investigate the morphology of two types of commercially used PTLs, sintered titanium and fiber titanium and analyzed their effect on oxygen transport in the channels. Both types of PTLs had a nominal thickness of  $250 \pm 5$   $\mu$ m. Fiber PTLs were found to have a higher porosity, larger pore sizes, and lower tortuosities than sintered PTLs, which translated into slightly lower overpotentials at 1 A cm<sup>-2</sup>. Furthermore, they studied two types of electrodes: catalyst coated membrane (CCM) and porous transport electrode (PTE) or gas diffusion electrode (GDE). Their modeling study predicted ionic conductivity limitations for GDEs which may cause the observed performance loss. To further understand the behavior of oxygen transport, Satjaritanun et al. [35] found evidence of oxygen taking preferential pathways on a pore-scale through the PTL at current densities up to 4 A cm<sup>-2</sup>. Most of the studies mentioned here focused on understanding interfaces and gas transport under constant anodic catalyst loading.

In this study, we present detailed investigation of the effect of the loadings on the performance of PEMWE with two different electrode configurations: catalyst coated membrane (CCM) and gas diffusion electrodes (GDE) using commercial IrOx electrocatalyst. We used x-ray CT to quantify the interfaces and x-ray radiography to observe oxygen transport in the channels. We then correlate the triple phase contact area

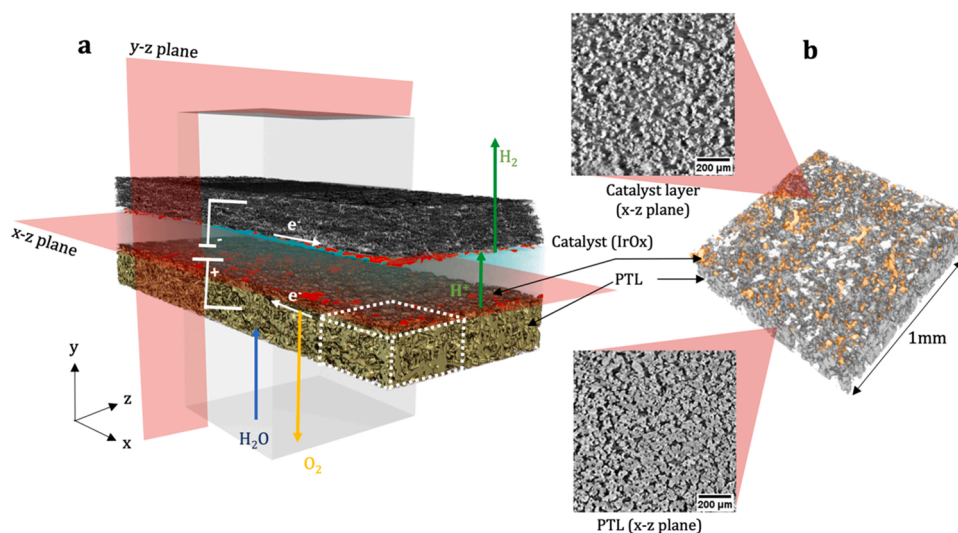


**Fig. 1.** a) Complete 3D volume rendering of a PEMWE obtained from x-ray CT showing all the components and the transport processes, b) 3D rendering of the representative cross section of the anode used for the purpose of this investigation. The blown-out regions show the 2D tomographs of the catalyst layer and the PTL as seen from the x-z plane. The catalyst shows up bright from the surrounded grayscale and hence can be segmented easily.

(TPCA) with the double layer capacities and identify proton and electron transport limitations with the help of Tafel analysis. Finally, we investigate the durability of these electrodes by applying steady state current holds and address the question on how to improve interfaces in existing PEMWE to elicit maximum performance for low catalyst loadings and how PTL morphologies can be tuned with respect to Ir loadings to utilize maximum gas transport pathways at high current densities.

## 2. Materials and methods

### 2.1. Electrolyzer Materials

Electrolyzer configurations with varying loadings were prepared for x-ray imaging, as well as electrochemical characterization. Table 1 lists the cell names and the type of PTL used, electrode configurations (CCM or GDE) and their respective catalyst loadings. Based on the loadings, the cells are segregated into three categories: i) high loadings of  $1.75 \text{ mg cm}^{-2}$  –  $2.20 \text{ mg cm}^{-2}$ , ii) medium loadings of  $1 \text{ mg cm}^{-2}$  –  $1.26 \text{ mg cm}^{-2}$ , iii) low loadings of  $0.5 \text{ mg cm}^{-2}$  –  $0.65 \text{ mg cm}^{-2}$ . Sintered and fiber Ti PTLs were provided by NEL (Wallingford, CT). For CCM configuration the PTLs were not coated by the catalyst, whereas for the GDE configuration the PTLs were coated by iridium based (IrOx) ink in a proprietary procedure by NEL with the loading indicated in the table. For both anode and cathode inks Nafion ionomer solution (1100 EW, 5 wt% ionomer; D521 from Ion Power, USA) was used. The CCMs were fabricated with a single pass screen printing technique to deposit the catalyst ink directly on the membrane surface and the GDEs were coated using an ultrasonic spray coater. GDEs used an ionomer to carbon (for Pt/C) and ionomer to IrOx weight ratios of 1.0 and CCMs used a weight ratio of 0.5. For all the GDE configurations, Toray TGP-H-120 carbon paper was used on the cathode side. Toray paper was coated by catalyst loading of  $2 \text{ mg cm}^{-2}$  of ink containing Pt/C. Nafion 117 from Fuel Cell Store (College Station, TX) was used in all the experiments as a membrane.

Six distinct x-ray *operando* cells with  $1 \text{ cm}^2$  active area were built for x-ray characterization and were used at 3 different beamtimes for ease of experimentation as well as swiftness in testing. Our previous work describes the design and development of these high-performance *operando* cells in detail [36]. All the cells were preconditioned by break-in procedure including five linear sweep voltammetries from 0 to  $5 \text{ A cm}^{-2}$  and

then holding the cells at  $1 \text{ A cm}^{-2}$  for 30 min at  $60^\circ\text{C}$  prior to imaging. The polarization curves collected at the beamline are reported in Fig. S1. Fig. S2 indicates the EIS spectra of the conditioned cells as tested at the beginning of life. The HFR of the preconditioned cells was ensured to be  $0.2\text{--}0.35 \text{ Ohm cm}^2$  during lab testing, but additional wiring during beamtimes can induce slight electrical resistance. However, this does not affect oxygen saturation in the channels at an applied current density. Additionally, there is no beam damage during the scan time which is previously reported in literature [30] and the before and after polarization curves were the same.

### 2.2. Electrochemical characterization

Electrochemical testing was performed at NEL Hydrogen using multi cell stacks at  $50^\circ\text{C}$  temperature. Catalysts used for the fabrication of both the CCMs and GDEs were iridium oxide and platinum black for the anode and cathode electrodes, respectively. For MEAs fabricated as CCMs, the anodes were coated using an electrode transfer process after being deposited onto a Teflon substrate. GDEs were manufactured by spraying ink onto the PTL, using an ultrasonic coater. To isolate the changes associated with the PTL construction and loading of the anode, all cathodes were processed as GDEs and spray coated onto a single sheet of carbon paper, in which the smaller test parts were cut from. Test parts were assembled into one of Nel's commercial cell hardware containing 3 cells with a total  $28 \text{ cm}^2$  active area (Fig. S3). Loading for the cathode was  $2.0 \text{ mg cm}^{-2}$ . These were selected to leverage proven stable cell design and because of the cell stack ability to handle multi-cell testing. Using this hardware, multiple cells could be tested at the same time, under the exact same conditions, making data more easily compared. Tests were conducted on one Nel's R&D test stands, with the same location used for all operational tests. The test stands are designed as a subscale version of Nel's commercial systems to simulate what would be expected in a fielded electrolyzer. All tests were allowed to reach the steady-state operating temperature of  $50^\circ\text{C}$  and 30 bar  $\text{H}_2$  pressure before collecting data. Polarization curves at 30 bar differential  $\text{H}_2$  pressure were collected up to  $2 \text{ A cm}^{-2}$  for beginning and end of life. All polarization curves were measured twice to ensure repeatability of the data. All samples processed and fabricated for the before mentioned operational tests were made in duplicate, with the second set of samples sent to University of California, Irvine for further characterization.

### 2.3. Tafel analysis

The Tafel analysis and the double layer capacitance measurements were conducted using a Gamry 5000 potentiostat. The test station used was an in-house made test rig comprising of a DI water heating and water recirculation system, and a repurposed Scribner fuel cell holder. The cathode bipolar plate was a standard graphite triple serpentine flow field, and the anode bipolar plate was a custom-made parallel channel ( $0.5 \text{ mm}$  land and channel dimensions) titanium flow filed with a plat-inized surface to reduce ohmic losses due to Ti passivation.

A  $5 \text{ cm}^2$  active area was used for electrochemical measurements. Before any electrochemical testing, the cell was heated to  $80^\circ\text{C}$  using cartridge heaters. DI water at  $80^\circ\text{C}$  was circulated through the anode at  $5 \text{ mlpm}$  for 30 min for the cell to heat up and the membrane to achieve adequate hydration. The cell temperature was maintained by using a k-type thermocouple and a PID temperature controller. The cell was then conditioned by applying chrono potentiometric hold of  $1 \text{ A cm}^{-2}$  for 30 min for the cell operation to be reproducible during the testing interval.

The Tafel slopes were recorded by chronoamperometric holds from  $1.3 \text{ V}$  to  $1.65 \text{ V}$  (iR free) with an increment of  $10 \text{ mV}$ . Each hold had a duration of 5 min to ensure a stable current draw. The slopes were then plotted by taking the average of the points recorded in the last one minute in the potential hold interval and on a semi log current density on the x-axis.

**Table 1**  
Electrolyzer configurations for x-ray CT and electrochemical characterization.

Sample #	Cell name	Fiber PTL	Sintered PTL	CCM	GDE	Loading ( $\text{mg cm}^{-2}$ )
1	Fiber CCM $0.5 \text{ mg cm}^{-2}$	✓		✓		0.5
2	Fiber CCM $1 \text{ mg cm}^{-2}$	✓		✓		1
3	Fiber CCM $2 \text{ mg cm}^{-2}$	✓		✓		2
4	Sintered CCM $0.5 \text{ mg cm}^{-2}$		✓	✓		0.5
5	Sintered CCM $1 \text{ mg cm}^{-2}$		✓	✓		1
6	Sintered CCM $2 \text{ mg cm}^{-2}$		✓	✓		2
7	Fiber GDE $0.65 \text{ mg cm}^{-2}$	✓			✓	0.65
8	Fiber GDE $1.1 \text{ mg cm}^{-2}$	✓			✓	1.1
9	Fiber GDE $1.75 \text{ mg cm}^{-2}$	✓			✓	1.75
10	Sintered GDE $0.65 \text{ mg cm}^{-2}$		✓		✓	0.65
11	Sintered GDE $1.1 \text{ mg cm}^{-2}$		✓		✓	1.1
12	Sintered GDE $1.75 \text{ mg cm}^{-2}$		✓		✓	1.75

## 2.4. Measuring double layer capacities

For the double layer capacity calculations, the cell was purged with 5% dry H<sub>2</sub> on the cathode at 50 mlpm at ambient pressure to ensure a pseudo-steady reference electrode for electrolyzer operation. The cell was maintained at 80 °C and heated DI water at 5 mlpm was fed on the anode side. iR free cyclic voltammetry scans were performed via voltage sweep from 0.3 V to 1.5 V. For each cell, 5 different scan rates were used between 20 mVsec<sup>-1</sup> and 150 mVsec<sup>-1</sup> (Fig. S13 c depicts an example of CVs with different scan rates). The current densities at 1–1.2 V (potential at which the CVs have the least slope and no Faradaic reactions) were plotted vs. scan-rates and the slope of the fitted line in this plot gives us the double layer capacity (Fig. S4, S5).

## 2.5. X-ray CT imaging

X-ray micro-tomography and radiography experiments were conducted at Beamline 8.3.2 at the Advanced Light Source (ALS) at Lawrence Berkeley National Laboratory and Beamline 2-BM-A at Advanced Photon Source (APS) at Argonne National Laboratory. At ALS, the image acquisition was performed at a beam energy of 25 keV selected using a double multilayer monochromator. Using a 20 μm LuAgB scintillator, an optical magnification of 4X, the images were captured by a sCMOS PCO Edge camera. This resulted in a spatial resolution of 1.16 μm pixel<sup>-1</sup>. The tomography scans were conducted at an exposure time of 300 ms per projection. An average of 1500 projections were collected for 180 degrees of sample rotation resulting in a total scan time of 9 min (including bright field background acquisition and optical adjustments) for tomography.

At APS, the image acquisition was performed at a beam energy of 27 keV selected using a double multilayer monochromator. Using a 20 μm LuAgB scintillator, an optical magnification of 5X, the images were captured by a sCMOS PCO Edge camera. This resulted in a spatial resolution of 1.73 μm pixel<sup>-1</sup>. The tomography scans were conducted at an exposure time of 150 ms per projection. An average of 1500 projections were collected for 180 degrees of sample rotation.

For X-ray radiography imaging, chronopotentiometric holds were applied for different current densities on the *operando* cell and the projections were acquired at an exposure time of 5 ms in both cell in-plane and through-plane directions. In this case, in-plane is defined when the x-rays pass parallel to the MEA and through plane is defined, as when they pass perpendicular to the MEA. Smaller exposure time allows observation of the oxygen transport in the channel especially at high current densities when gas formation and transport is very rapid. However, smaller exposure time also resulted in low signal-to-noise ratio making it difficult to segment oxygen from water while image processing. For this experiment, 5 ms acquisition time per projection was ideal to achieve a reasonable signal-to-noise ratio, while also capturing the rapid oxygen transport.

## 2.6. Image processing and visualization

The tomography image datasets were reconstructed using TomoPy [37] and Gridrec algorithm. Our earlier works report parameters and details of the reconstructions [38,39]. The reconstructed images were further processed using Fiji ImageJ. The images were converted to 8-bit, cropped and thresholded manually. The thresholded catalyst, PTL and other parts were visualized in 3D using ORS Dragonfly. PTL porosities and pore size distributions were calculated by using imageJ macros and plugins. The tortuosity factors were calculated using MATLAB's Tau-Factor application. Subsequently, we attempted to calculate the catalyst loadings for all the cells by using the thresholded catalyst images as depicted in Fig. S6. The total volume of the catalyst was calculated using the ImageJ plugin BoneJ. This volume was then multiplied with catalyst density to obtain the total mass which was then divided by the area to give the loadings in mg cm<sup>-2</sup>. It is important to note that the loadings

obtained by this method may not be completely accurate since catalyst particles smaller than the limit of resolution of micro x-ray CT may not be captured and human error contributes to overall thresholding error. Nevertheless, the obtained values can give us a rough estimate of the true loading and hence help validate the ensuing data.

## 2.7. Interface analysis and oxygen content calculations

Our previous work details the interfacial analysis of the two types of electrolyzer configurations [30]. That is, the GDE vs CCM for sintered and fiber titanium PTL. The purpose of interfacial analysis is to quantify the triple phase contact area (%TPCA) at the anode side. Since the catalyst materials attenuate x-rays highly due to their higher atomic weight and density, they appear perceptively bright in absorption contrast x-ray imaging. For each sample, 1 mm × 1 mm representative areas were selected and the catalyst and PTL were thresholded manually. It is crucial to capture all the catalyst pixels and segment them from the remaining greyscale to report the %TPCA values accurately. Hence during the thresholding process, only the areas having greyscale values between 250 and 255 (255 being the brightest feature) were selected and everything else was '0'. The reason for choosing an interval over a single value was to capture all the catalyst pixels that lie within the statistical limit of imaging process and hence this scheme was kept consistent across the entire sample pool.

Once the phases were thresholded, a 2D interfacial projection was generated by summing all slices within ~ 5 μm of the interface in the through-plane direction. This ensures that the surface roughness is captured, as well as swelling of the membrane into the PTL during PEMWE operation [9]. For this investigation, we assume that the ion conduction media, that is, the membrane or the ionomer is present at all places surrounding the PTL and the catalyst. Here, we define the equation of %TPCA as:

$$\%TPCA = \frac{\text{Area of catalyst phase}}{\text{Intercept area of two phases (PTL + Membrane)}} \times 100\% \quad (1)$$

where %TPCA is the triple phase contact area. The areas of the different phases are calculated by ImageJ using the corresponding 2-D projections. The following assumptions are made during the calculations:

i) the ion exchange media (ionomer) is present everywhere at the interfacial region and is considered as a 3D entity; ii) the membrane and catalyst layer are considered as 2D entities within the interfacial region.

For the oxygen content calculations, we used the radiography data with experimental conditions as detailed in the x-ray CT imaging section above. For consistency, we selected only the through-plane images for all the cells and normalized each image stack with the corresponding OCV image since no oxygen is produced at OCV. The OCV image was obtained by averaging 20 image slices at OCV conditions. This helps to remove most of the background and thus improves the contrast of oxygen. A representative region of interest (ROI) in the resulting image stack was selected in such a way that it encompassed maximum region of the channel at a selected location where the distortions are minimal. (as shown in Fig. 7c,f). Distortions may occur because of gaskets, leaking water, or other parts coming in the way of incident x-rays. The length of the ROI was kept as close to the channel depth as possible (~1000 μm) and the breadth was kept anywhere between 200 and 300 μm depending on image quality and noise. Subsequently, an ImageJ macro computed the average grayscale values in the ROI over the entire image stack consisting of about 3000 projections. The grayscale values corresponding to oxygen were determined manually by selecting an oxygen bubble in the image stack and measuring the average grayscale value over its length. At least 5 oxygen bubbles were selected and measured for grayscale values at random throughout the image stack and the obtained numbers were averaged to get a single threshold value for oxygen. The



ratio of the number of average values above this threshold to the number of total number of projections gives us the oxygen content at a given current density. The error bars were obtained by using the upper and lower oxygen grayscale value thresholds and calculating the corresponding oxygen contents.

## 2.8. Modeling

Direct modeling-based Lattice Boltzmann method (LBM) was used to simulate the oxygen transport through the PTL samples of sintered and fiber PTLs. LBM is a particles-based approach, which is appropriate for fluid flow simulations in the complex geometries such as porous structure of the PTLs and GDLs [40–42]. The Boltzmann transport equation was used to solve the mass transport in the computational domain. More details concerning the Boltzmann transport equation and the concept of LBM related to this model are discussed in the SM. In this work, commercial software XFlow 2020 (Refresh 1 Beta, build 108.07) was used to perform the numerical simulations. A 3D multiphase flow model combined with a time-dependent simulation was used to mimic the oxygen transport inside the PTL samples for PEMWE. The lattice size (i.e., grid or particle size) of these simulations was set at  $1.00\ \mu\text{m}$ . The volume of the computational domain depended on the PTLs, as shown in SM Fig. S7. The time step of all simulations was set to 10 nanoseconds per time step. The simulation was calculated until the predictions reached steady-state or expected times.

In this work, the oxygen flux from the OER was assumed to be constant at the catalyst layer corresponding to the constant current density. The cell operating condition was set at  $1\ \text{A cm}^{-2}$  with the water flowrate of 2 sccm. The surface wettability of the PTL was assumed to be constant across the entire geometry surface at 50 degrees. The isothermal model was used in the simulations. The oxygen gas was fed into the computational domain from the top of the PTL where the catalyst layer is located. This oxygen inlet boundary condition was defined with a variety of configurations based on the model assumptions. To study the effect of the catalyst loading on the oxygen transport in the PTLs, the simulation was defined using three different model assumptions based on catalyst loading. For the high catalyst loading, the uniform catalyst coating was assumed. Therefore, the void area on the top of the PTL was determined to be the inlet surface boundary for oxygen. In the medium catalyst loading scenario, we assumed the catalyst coating is nearly uniform. 75% of the top void area was specified to be the inlet in this case. For low catalyst loading, we assumed that the catalyst coating is non uniform. Consequently, 50% of the void area at the top PTL area was chosen to be the inlet boundary of this model assumption. Note, that these selected percentages are not quantitative, but the simulations are used more in qualitative way to investigate whether catalyst uniformity impacts oxygen transport in the PTLs. For all three scenarios current was the same, therefore for the least uniform case the current density per catalyst site was higher than for the uniformly distributed catalyst. To observe the prediction of oxygen transport clearly in the PTL, the Z-Project plugin in the ImageJ program was used to create an average amount of oxygen content in the in-plane direction.

## 3. Results and discussion

### 3.1. Tomography data visualization

To study and quantify the interfaces within the PEMWE system, it is essential to first establish an understanding of the x-ray images and the representative areas. Fig. 1 shows the complete 3D volume rendering of the PEMWE cell and the representative cross sections required for this study. As shown in Fig. 1, the cell consists of a proton conducting membrane (Nafion 117) sandwiched between a Ti PTL anode and a carbon based GDL. The PTL carries liquid water to the anode catalyst layer from the underlying channels and draws out the product oxygen gas. Oxygen evolution reaction (OER) occurs at the anode catalyst layer

driven by the high applied potential vs. cathode. At the same time, HER occurs at the catalyst layer and the evolved hydrogen gas is drawn out through the GDL into the gas channel. The PTL and the catalyst layer interface play a crucial role in the overall PEMWE performance and hence will be the primary focus of this work. Fig. 1b shows the 3D volume rendering of the interfacial region (dotted region in Fig. 1a) and the PTL as seen from the x-z plane. All analysis was conducted on these representative  $1\ \text{mm} \times 1\ \text{mm}$  areas. The histogram, thresholded catalyst image and overlay between the thresholded and original image is shown in Fig. S8 in SM. The yellow portions in Fig. 1b represent the catalyst layer, and the grey areas represent the adjacent PTL. As discussed earlier, the catalyst shows up brighter than the PTL in the x-ray CT images as shown in the blown out 2D tomographs. The x-z plane was used for interfacial analysis and the y-z plane was used for radiography imaging to quantify the oxygen content in the water channels.

### 3.2. Visualizing electrodes with various catalyst loadings

The 2D reconstructed tomography slices at the interfacial region and the corresponding 3D volume rendering of the total catalyst were compared to better understand the effect of loadings and electrode configurations as shown in Fig. 2. The in-plane images (x-y plane) highlighting the selected representative areas are shown in Fig. S9. The overlay between the thresholded catalyst outlines and the original grayscale images for all representative cross sections is shown in Fig. S10. For the fiber CCM configuration (Fig. 2a), the catalyst distribution is sparse for the low loaded  $0.5\ \text{mg cm}^{-2}$  sample and gets denser as the loading is increased. For medium and high loaded samples, the degree of clustering and agglomeration is seen to increase with loading. Similar behavior was observed for sintered CCM samples (Fig. 2c). Although x-ray micro CT cannot capture catalyst particles under  $1\ \mu\text{m}$ , which is the limit of resolution [36], it can map localized particle agglomeration and portions of sparse loading. These heterogeneities limit geometric area and cause discontinuities in electrical percolation networks especially in loadings at or below  $0.5\ \text{mg cm}^{-2}$ .

These heterogeneities on the anode have a greater detrimental consequence as compared to the cathode because of two concurrent reasons: the fast kinetics of HER on Pt/C and the possibility to use high surface area carbon as a support, leading to well-dispersed and electrically stable electrodes. Hence it is important to tune the interface and improve the anode catalyst layer homogeneity to ensure maximum utilization of the available catalyst. Although ball milling, sonicating and other chemo-mechanical processes can reduce particle size and improve the stability and dispersion of ink, the coating and drying process can greatly influence the catalyst layer homogeneity for CCMs.

For GDEs, the catalyst was directly coated on the PTL. As shown in the Fig. 2b, the catalyst conformed to the fiber PTL surface morphology and the packing density increased with loading. For low loaded samples, discrete patches of catalyst were observed to accumulate on the top portion of the  $\sim 20\ \mu\text{m}$  fiber strands and the catalyst coating within the remaining curved surface area of the fibers was minimum. These discontinuities were reduced for the medium loaded samples as the catalyst occupied almost the entire top area and some of the curved surface area of the fibers. For high loaded samples, dense catalyst was seen throughout the surface area of the fibers and the catalyst also deposits coarsely on the adjacent layer of fibers. Similarly, for sintered GDEs, (Fig. 2e) the catalyst packing density increased with loading. However, as opposed to fiber PTL, sintered PTLs were made of interconnected Ti particles and the end surfaces were flat for smooth connectivity with the membrane and current collector. Hence, most of the catalyst was deposited on the flat surfaces during coating process and there was less catalyst penetration within the PTL.

Although it is apparent that CCMs showed a higher degree of catalyst clustering than GDEs, the catalyst layer homogeneity can be tuned by improving the water to solvents ratio in the ink, ink drying properties, or the coating process of the ink [43]. This degree of freedom cannot be as

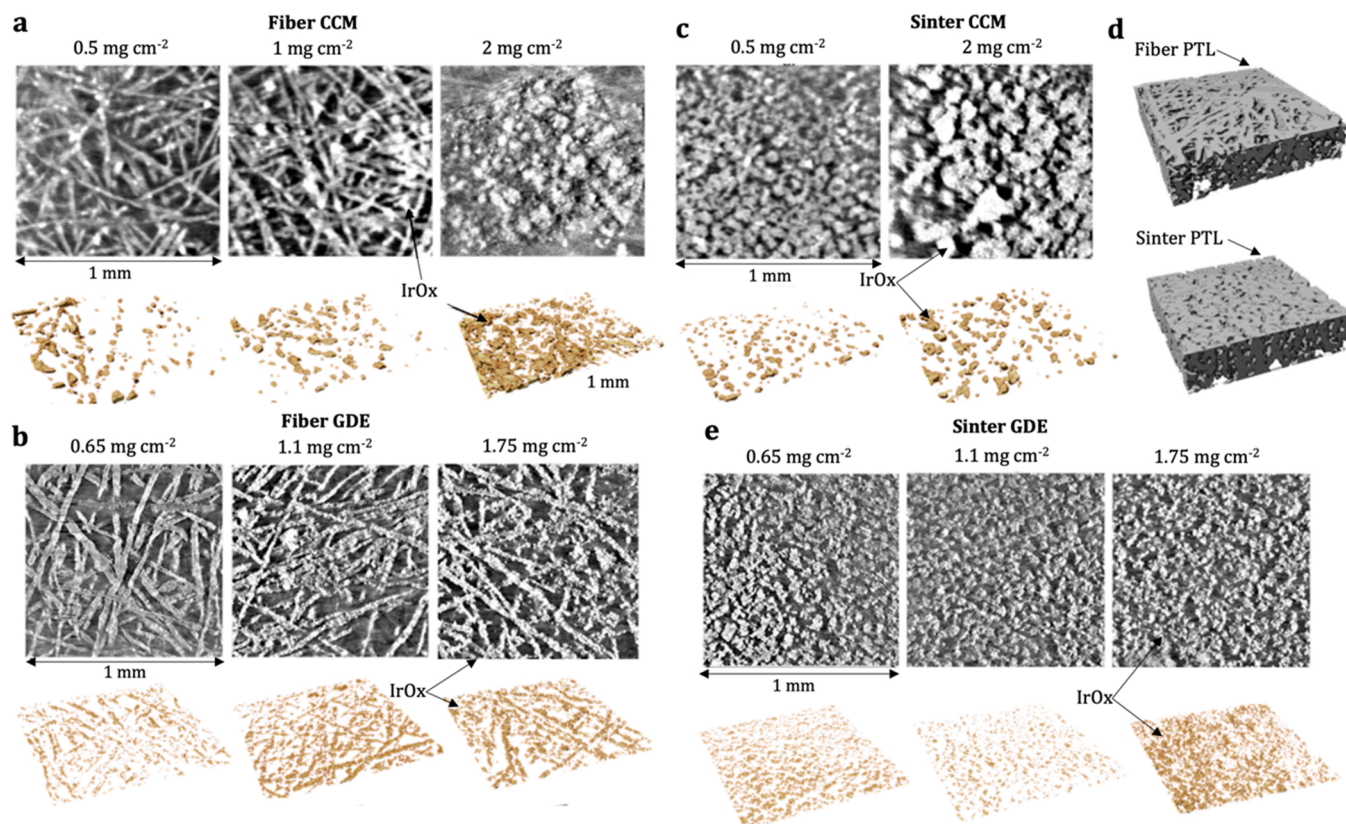


**Fig. 2.** 2D reconstruction and 3D renderings of catalyst and PTLs in different cells obtained from x-ray tomography a) Fiber CCM  $0.5 \text{ mg cm}^{-2}$ ,  $1 \text{ mg cm}^{-2}$  and  $2 \text{ mg cm}^{-2}$  b) Fiber GDE  $0.65 \text{ mg cm}^{-2}$  and  $1.1 \text{ mg cm}^{-2}$  and  $1.75 \text{ mg cm}^{-2}$  c) sintered CCM  $0.5 \text{ mg cm}^{-2}$  and  $2 \text{ mg cm}^{-2}$  d) sintered GDE  $0.65 \text{ mg cm}^{-2}$  and  $1.1 \text{ mg cm}^{-2}$  and  $1.75 \text{ mg cm}^{-2}$  e) 3D renderings of fiber and sintered PTLs.

well achieved when fabricating GDEs since the catalyst layer properties are also dictated by the surface morphology of the PTL. The catalyst layer homogeneity becomes increasingly important for reduced catalyst loadings for the following reasons: i) higher loadings can circumvent poor in-plane electrical percolation networks [44–46], ii) higher catalyst contact area with PTL and membrane leads to better %TPCA and reduces interfacial contact and catalyst layer electron transport resistances.

While the electrochemically active surface area (ECSA) can be easily calculated for Pt-based electrodes because of the hydrogen underpotential deposition fingerprint [47,48], it is ineffective for IrOx based electrodes. Hence, ECSA for IrOx based electrodes is determined either from known specifications or experimentally using mercury underpotential deposition [49] or zinc adsorption [50]. These techniques present challenges in application for working PEMWE cells. ECSA is measured at low current densities, whereas many of the sites calculated to be active under ECSA measurements can become inactive under higher current densities, where transport cannot be neglected. The %TPCA in PEMWE is dictated by the localized hydration-based swelling of the membrane into the PTL and the irregularities in compression due to surface roughness of the PTL-catalyst layer interface. X-ray CT provides unfettered access into the operating PEMWE cell interfaces and provides an alternative measure of the ECSA, relying on geometry. The values of the %TPCA obtained for all the cell configurations from Table 1 were reported in Fig. S11. The nature of the interfaces in different electrode configurations can be better understood by calculating the anodic double layer capacities.

Fig. 3 shows the double layer capacities ( $C_{dl}$ ) obtained for all four electrode configurations with varying loadings. It also correlates the double layer capacitance with the %TPCA. Primarily,  $C_{dl}$  represents interface between IrOx and water and is an indirect measure of

electrocatalyst surface area. Generally, for CCMs (Fig. 3a) one observes the trend of specific double layer capacity decrease with decrease in IrOx loading. This is expected, as with lower loading lower surface area of catalyst translates into lower double layer capacitance. We also report mass-normalized double layer capacitances in SM, Fig. S12. For the high loaded CCMs (Fig. 3a), sintered CCMs show about  $0.3 \text{ F cm}^{-2}$  higher average  $C_{dl}$  value than their fiber counterpart. This is substantiated by the fact that high loaded sintered CCM showed almost 20% higher TPCA. Fiber CCMs showed large standard deviation in double layer capacity values. The difference between  $C_{dl}$  of sinter and fiber CCM is due to porosity of PTLs near the interface with the catalyst layer but also catalyst agglomeration observed for fiber PTL. In contrast, we observed a 20% higher TPCA for sintered PTL owing to its low porosity (47%) (Fig. S16) and good contact with the catalyst layer. The values for  $C_{dl}$  are almost identical between the sintered and fiber PTLs for medium and low loaded CCMs. At  $1 \text{ mg cm}^{-2}$ , sintered CCMs still show about 10% higher TPCA than their fiber counterpart. However, at low loadings, sintered CCMs show only  $\sim 3\%$  higher TPCA. The  $C_{dl}$  as a function of %TPCA for CCMs was plotted in Fig. 3c. Generally, a linear trend was observed between the %TPCA and double layer capacitance, indicating that both methods show similar type of information.

Fig. 3b shows the  $C_{dl}$  values for GDEs. Again, generally, with the decrease in loading the double layer capacity values also decrease, except for  $1.75 \text{ mg cm}^{-2}$  having lower average  $C_{dl}$  compared to  $1.1 \text{ mg cm}^{-2}$  for sinter GDE. For high loaded  $1.75 \text{ mg cm}^{-2}$  samples, fiber GDE shows about  $12 \text{ mF cm}^{-2}$  higher  $C_{dl}$  value than its sintered counterpart. This can again be explained by the fact that fiber GDE shows about 20% higher TPCA than its sintered counterpart. For medium and low loaded GDEs, the difference in  $C_{dl}$  between fiber and sinter GDEs is within the  $2 \text{ mF cm}^{-2}$  range as shown in Fig. 3d. The substantially higher %TPCA and  $C_{dl}$  for fiber GDE at high loadings can be due to the

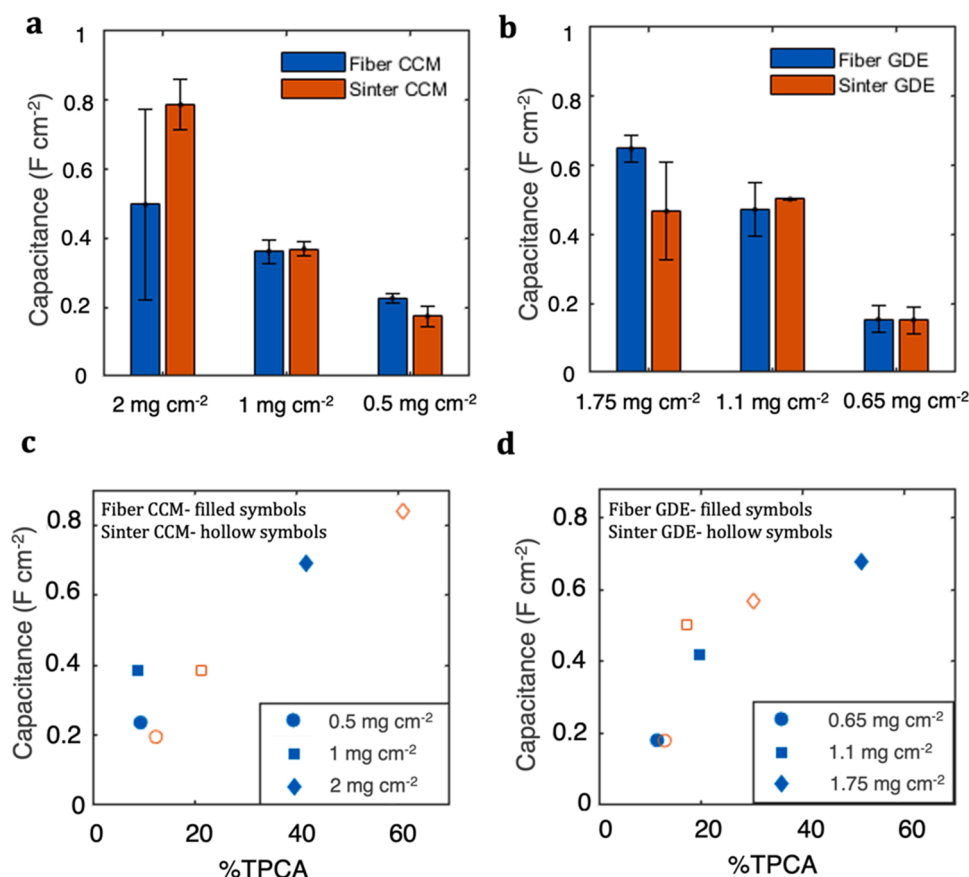


**Fig. 3.** a) Double layer capacities of fiber and sintered CCMs for high, medium and low loadings, b) double layer capacities of fiber and sintered GDEs for high, medium and low loadings Average double layer capacitance plotted against % TPCA for c) CCMs and d) GDEs, respectively.

increased coverage of the catalyst over the curved surface area of the fibers as opposed to only the flat surfaces in sintered GDE. However, as the loading reduces to 1.1  $mg\ cm^{-2}$  we observed a slight increase in  $C_{dl}$  for sintered GDE. Although this could be due to a nucleating oxygen bubble or residual gas in the PTL masking the catalytic site, the local heterogeneities in the catalyst layer could also affect the measurements. GDEs at low loadings of 0.65  $mg\ cm^{-2}$  show almost identical  $C_{dl}$ , although sintered GDE shows a 2% higher TPCA, it is inadequate to affect the  $C_{dl}$  substantially. Again, almost linear trend is observed for

double layer capacitance vs. %TPCA for fiber and sintered GDEs, with 1.1  $mg\ cm^{-2}$  sample being outlier.

Comparing the high loaded fiber CCMs and GDEs, fiber GDE shows over 10  $mF\ cm^{-2}$  higher  $C_{dl}$  and concomitantly  $\sim 10\%$  higher TPCA than fiber CCM. A reasonable explanation for these observations could be that in fiber GDE compared to fiber CCM, the catalyst has a greater surface area due to the surface roughness of the PTL. Another reason could be that imaging results is an underestimation of the TPCA especially for high loadings due to resolution limits. However, in case of high loaded

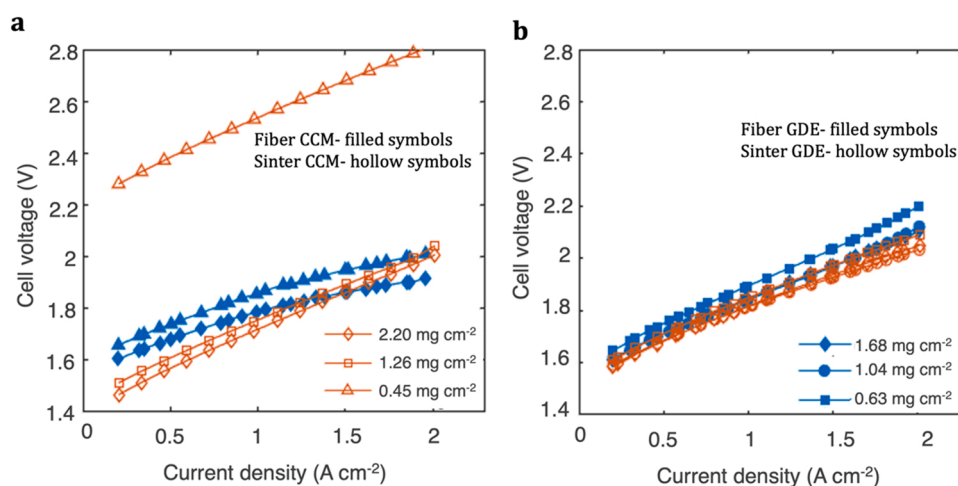


**Fig. 4.** BOL polarization curves for a) fiber and sintered CCMs, b) fiber and sintered GDEs. The tests were conducted at 50 °C in a 28  $cm^2$  active area cell using a Nafion 117 membrane. Cathode Pt loadings were kept at 0.2  $mg\ cm^{-2}$  for all tests. The filled symbols represent fiber PTLs, and hollow symbols represent sintered PTLs.



sintered electrodes, sintered CCM show a substantial  $30 \text{ mF cm}^{-2}$  higher  $C_{dl}$  and concomitantly  $\sim 30\%$  higher TPCA than sintered GDE. In this case, because of the low porosity of the PTL, the catalyst is deposited mostly on the surface of the sintered PTL causing agglomeration. Hence, the exposed area of the catalyst was lower as compared to CCM resulting in smaller  $C_{dl}$ .

### 3.3. PEMWE performance

Fig. 4 shows the measured beginning of life (BOL) polarization curves for all the samples. Cell performance for fiber and sintered CCM at low, medium, and high loadings are shown (Fig. 4a). Similarly, cell performance for fiber and sintered GDE at low, medium, and high loadings is plotted (Fig. 4b). There is a slight difference in loadings that were used for x-ray characterization and electrochemical testing since the experiments were conducted separately by UCI and Nel Hydrogen.

The polarization performance at current densities up to  $1.5 \text{ A cm}^{-2}$  can be related to the  $C_{dl}$  vs TPCA parameter space. The most notable detail of the CCM polarization curves is the better performance because of high TPCA and  $C_{dl}$  for high loaded sintered electrodes followed by medium loaded sintered electrodes. In comparison, high loaded fiber CCM show over 100 mV higher overpotential compared to sintered CCM at current densities below  $0.5 \text{ A cm}^{-2}$  suggesting limitations in OER kinetics stemming from anodic interfacial area. No significant performance drop was observed for medium loaded sintered CCM although there is significant decrease in %TPCA and  $C_{dl}$  compared to high loaded CCM configuration. At low loadings, fiber CCM shows an 800 mV improvement compared to its sintered CCM counterpart which is surprising, since there is no significant difference in TPCA and  $C_{dl}$  between these two configurations. The poor performance of these sintered CCMs can arise from low %TPCA, but we cannot rule out the possibility of some other factors at play here. One of them can be the inhomogeneity of the catalyst layer revealed by XRF mapping pictured in Fig. S19. Another reason could be the hydrogen crossover because of 30 bar differential operation. The crossed over hydrogen renders some catalytic sites inactive and possibly PTL cohesion issues that may be overcome with the use of an MPL.

The performance of all sintered GDEs was apparently similar until

$1.5 \text{ A cm}^{-2}$ , which is surprising, since we expected performance loss in lower loaded samples due to lower available double layer capacity of about  $30 \text{ mF cm}^{-2}$  than medium and high loaded samples. However, there was only 5–10% difference in the TPCA between the medium and low loaded samples, which suggests that contact areas between PTL, catalyst layer and membrane were similar. The performance of fiber GDEs was also similar to sintered GDEs for high and medium loadings as seen in Fig. 4b. However, low loaded fiber GDEs show a 100 mV increase in overpotential than high and medium loadings due to increasing contribution of mass transport overpotential at  $2 \text{ A cm}^{-2}$ .

We found that GDEs typically have a poorer performance than their CCM counterparts at similar loadings, which is consistent with our earlier work [30]. At low current densities of  $10 \text{ mA cm}^{-2}$ , where the overpotential is described by kinetics, higher loaded sintered CCMs show approximately 200 mV improvement than their corresponding GDEs. This is a substantial potential difference since kinetic overpotential contributes significant two thirds to the total overpotential until  $2 \text{ A cm}^{-2}$  [51]. This suggests possible proton or electron transport limitations at the interface.

### 3.4. Tafel analysis

To better understand the reaction mechanisms at low current densities, the Tafel plots for fiber CCM and GDE (Fig. 5a,c), sintered CCM and GDE (Fig. 5b,d) are presented and slopes were displayed (Fig. 5e). The associated CVs and slopes are reported in Fig. S4 and Fig. S5 for GDEs and CCMs, respectively. The Tafel slopes were obtained by a linear regression on the semi-logarithmic plot of  $iR$ -free cell voltage. The regression lines were plotted for points below  $100 \text{ mA cm}^{-2}$  assuming this as the kinetically dominated region for all cells. The Tafel slopes obtained for CCMs are within the range of  $57.6 \text{ mV dec}^{-1}$  to  $64.3 \text{ mV dec}^{-1}$ , which are in good agreement with the values reported in literature for unsupported  $\text{IrOx}$  based catalysts in acidic medium up to  $70^\circ\text{C}$  [46], [51–53]. The Tafel slope  $b$  is empirically defined as  $2.303RT/\alpha F$  and the total kinetic overpotential  $\eta_k$  as a function of the Tafel slope is given by  $\eta_k = \log(j/j_0)$ . Here  $R$  is the universal gas constant,  $T$  is the absolute temperature,  $\alpha$  is the electron transfer coefficient,  $F$  is the Faraday's constant,  $j$  is the current density and  $j_0$  represents the exchange current

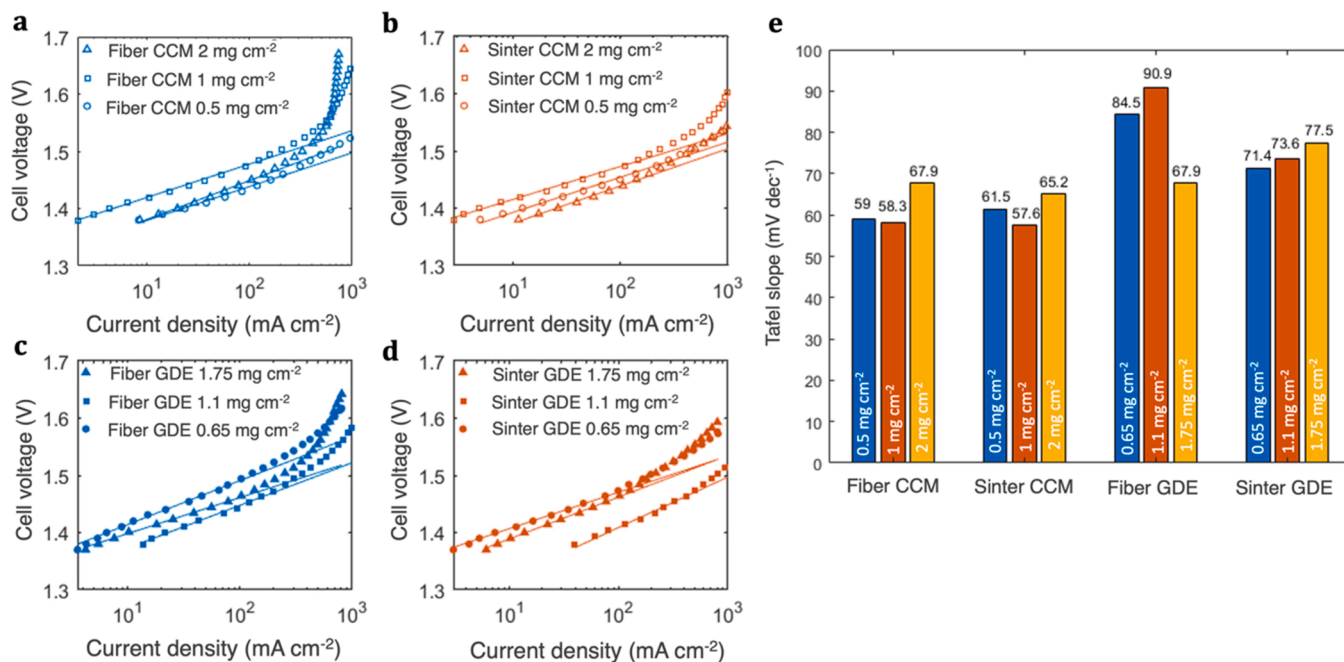


Fig. 5. Experimentally obtained Tafel plots for a, b) fiber and sintered CCMs respectively c, d) fiber and sintered GDEs respectively e) tabulated Tafel slopes for all configurations and loadings. All Tafel slopes were collected at  $80^\circ\text{C}$  in a  $5 \text{ cm}^2$  active area cell.



density. Hence the Tafel slope was directly proportional to the absolute temperature, and the total kinetic overpotential is dependent on the exchange current density. However, this is a simplified theoretical derivation of the Tafel slope, which assumes the coverage of the reaction intermediate species in the reaction progress as constants. When the

actual surface kinetics are considered, the Tafel slope also depends on the surface oxides coverage [54], the nature of the electrode and the interface leading to dynamic utilization of the catalyst, which has been previously reported and substantiated in literature [28].

For fiber GDEs the Tafel slope show a decreasing trend with increase

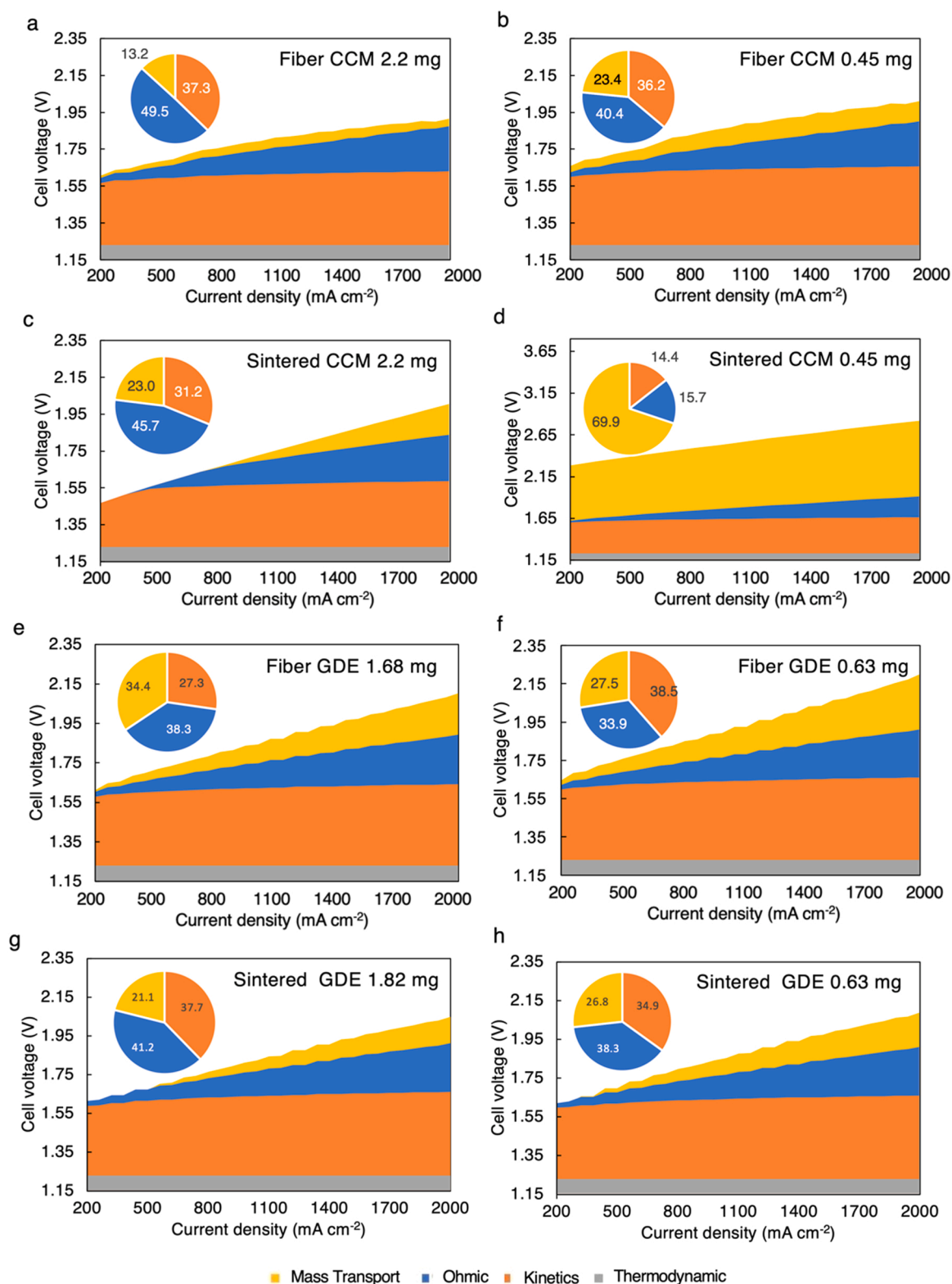


**Fig. 6.** Overpotential breakdown of polarization curves into thermodynamic, kinetic, ohmic and mass transport and other contributions for a) fiber CCM  $2.2 \text{ mg cm}^{-2}$ , b) fiber CCM  $0.45 \text{ mg cm}^{-2}$ , c) sintered CCM  $2.2 \text{ mg cm}^{-2}$ , d) sintered CCM  $0.45 \text{ mg cm}^{-2}$ , e) fiber GDE  $1.68 \text{ mg cm}^{-2}$ , f) fiber GDE  $0.63 \text{ mg cm}^{-2}$ , g) sintered GDE  $1.82 \text{ mg cm}^{-2}$ , h) sintered GDE  $0.63 \text{ mg cm}^{-2}$ . Inset pie charts show the percentage overpotential share at  $1.5 \text{ A cm}^{-2}$ .

in loading. The recorded Tafel slope for low loaded sample was 76.8 mV dec<sup>-1</sup> and it steadily decreased to 74.7 mV dec<sup>-1</sup> for medium loaded sample and finally the high loaded sample show the lowest slope of 62.9 mVdec<sup>-1</sup> as reported in Fig. 5c and e. This trend is consistent with that reported in literature [28,29] since higher loadings facilitate better kinetics. However, this trend was not followed by the CCMs, since we observed a dip in the in Tafel slope from 61.5 mV dec<sup>-1</sup> for low loaded sintered CCM to 57.6 mV dec<sup>-1</sup> for medium loading and an apparent rise to 63 mV dec<sup>-1</sup> for high loaded sample. The same trend was observed for fiber CCMs. Sintered GDEs show an increase in Tafel slope from 63.6 mV dec<sup>-1</sup> to a fairly constant 73 mV dec<sup>-1</sup> for medium and high loaded samples. While the TPCA shows a consistent rise with loading for all CCMs and GDEs, the discrepancy in Tafel slopes between different loadings is unlikely to be due change in the reaction mechanisms, but likely due to factors like nature of the electrode, the catalyst layer homogeneity, catalyst layer utilization and increased mass transport resistance [25,55].

It is important to note that for similar loadings, GDEs consistently show a higher Tafel slope than their CCMs counterpart. Low loaded fiber CCM and fiber GDE have a Tafel slope difference of nearly 18 mV dec<sup>-1</sup>. However, this difference reduces as the loadings increase suggesting that the underlying mass transport losses or conductivity limitations negatively affect the reaction kinetics, as the loadings are reduced below 0.5 mg cm<sup>-2</sup>. Between similar loaded CCMs, the Tafel slope difference remained within  $\pm 2$  mV dec<sup>-1</sup> even though the TPCA difference between high loaded fiber and sintered CCM was  $\sim 20\%$ . For GDEs, we observed Tafel slope difference of nearly 13 mV dec<sup>-1</sup> between the lowest loaded samples but a TPCA difference of only  $\sim 3\%$ .

### 3.5. Overpotential breakdown

To further understand the contributions of different overpotentials to the total cell potential, the BOL polarization curves were fitted using a 0D model. The parameters and equations used to fit the curves can be found in the Table S1 in the SM. The total cell voltage,  $E_{cell}$  is the sum of the thermoneutral voltage and associated voltage losses:

$$E_{cell} = E_{rev} + \eta_{kin} + \eta_{\Omega} + \eta_{mt} \quad (3)$$

where  $E_{rev}$  is the thermoneutral voltage,  $\eta_{kin}$  is the kinetic overpotential for OER,  $\eta_{\Omega}$  is the Ohmic overpotential and  $\eta_{mt}$  is the mass transport overpotential. Eqs. S1-S5 show the calculations to obtain each of these potentials. The mass transport overpotential is the remainder. The cathode kinetic overpotential is neglected in this analysis. Fig. 6 presents the overpotential breakdown for high and low loaded electrode configurations. The kinetic overpotential was calculated by using the Tafel slopes and the TPCA values obtained from electrochemical characterization and imaging, respectively (Eq. S5). Fig. S13 in SM depicts the bar plot of overpotentials breakdown at 1.5 A cm<sup>-2</sup> for all the cells. The kinetic overpotential is the major contributor especially at current densities below 1 A cm<sup>-2</sup> and its total share was observed to increase monotonically across the full current density range with decrease in catalyst loading. An increase in the TPCA results in lower kinetic overpotential and decrease in Tafel slope results in lower kinetic overpotential. Peng et al. [31] show the variation of kinetic overpotential with interfacial contact area for low loaded electrodes and attribute the trends to two main limiting factors: in-plane electron transport and catalyst accessibility.

It is worth mentioning that the ohmic share in this set of computations was obtained by using the membrane conductivity since the HFR values were unavailable. However, it is safe to assume that the electrical contribution to the HFR was constant since all the tests were conducted in similar cell hardware on the same test stand. Since mass transport overpotential was the remaining overpotential, after calculating kinetic and ohmic transport overpotentials it also might include additional overpotentials that are not accounted by ohmic and kinetic losses.

For fiber CCMs (Fig. 6a-b) kinetics occupied over 40% of the total overpotential at 1.5 A cm<sup>-2</sup>, however, mass transport starts to dominate as the IrOx loading decreased, and we see an apparent decrease in the percentage of kinetic share with decrease in loading. Low loaded sintered CCMs had a significant increase in mass transport, as compared to their high and medium loaded counterparts (Fig. 6c-d). This is rooted in the gas transport through the PTL and the channel discussed in the following sections. Low loaded GDEs had a higher kinetic overpotential at any given current density than their CCM counterparts. For example, at 1.5 A cm<sup>-2</sup> and low loadings, fiber GDE had a 45 mV higher kinetic overpotential than its CCM counterpart, whereas sintered GDE had a  $\sim 5$  mV higher kinetic overpotential than its CCM counterpart. In terms of the mass transport and additional overpotentials, the values depend on several factors, but we will be confining ourselves to their dependence on TPCA and PTL morphology, since we believe that these are the most significant contributors. The mass transport and other overpotentials increased with decrease in catalyst loading. In terms of the absolute potentials, we observed a higher mass transport loss in GDEs compared to their CCM counterparts (Fig. 6e-h), except for low loaded sintered electrodes.

### 3.6. Investigating mass transport losses

Mass transport losses are the major contributor to the PEMWE overpotential at high current densities, especially at low IrOx loadings and are greatly influenced by the interfacial characteristics and the PTL morphology. High and medium loaded CCMs show an average 100 mV lower overpotential than their GDE counterparts at 1.5 A cm<sup>-2</sup>. In general, we saw substantial mass transport limitations for low loaded samples especially at the EOL, as will be discussed later. Hence interfaces and the PTL morphology have a greater significance at reduced loadings. Fig. S14 in SM represents mass transport and kinetic overpotentials as a function of TPCA at 1.5 A cm<sup>-2</sup> for CCMs and GDEs. The TPCA calculated earlier (Fig. 3) is in direct relation to the mass transport characteristics since a higher TPCA relates to larger number of reaction sites and concomitantly higher number of bubble nucleation sites for oxygen. This also results in reduced kinetic overpotentials. For sintered CCMs, the kinetic overpotential reduces by over 50 mV when the TPCA increases from 12% to 60%. Similar trends are observed for GDEs. At higher TPCAs both CCM configurations showed reduction in mass transport overpotential, whereas no clear correlation was observed between the TPCA and mass transport overpotential for GDE configurations (Fig. S14). The nature of the electrode structure and its hydrophobicity also influences the gas transport [56]. Kadyk et al. [57] developed a structure based model to optimize gas evolution in electrolyzers and concluded that having preferential nucleation sites on the surface of the electrode leads to easier gas removal into the surrounding electrolyte (water) and reduces the mechanical stress leading to catalyst degradation or destruction.

In terms of the PTL morphologies, sintered PTL had a lower porosity (44.7%) than fiber PTL (56.5%). The porosity profiles of both samples were shown in Fig. S15. The pore-size distribution of these samples were reported in Fig. S16 showing significantly lower average pore size (radius) for sintered PTL of 8.1  $\mu$ m compared to fiber PTL of 13.3  $\mu$ m. The in-plane and through plane tortuosity factors for both PTLs can be found in the SM Fig. S17. The in-plane tortuosity factors were higher in general than through plane values and the void pathways were more tortuous than the solid pathways for both PTLs as reported earlier [30]. For fiber PTLs, the in-plane tortuosity was found to be higher (2.7) than sintered PTLs (2.56). However, the through plane tortuosity for sintered PTLs was slightly higher than fiber PTL but still within the statistical limit of measurement. The through-plane tortuosity is a critical morphological parameter as it dictates oxygen removal from the catalyst layer into the flow channel.

To quantify the gas transport in these configurations and understand its impact on PEMWE performance, we analyzed x-ray radiography

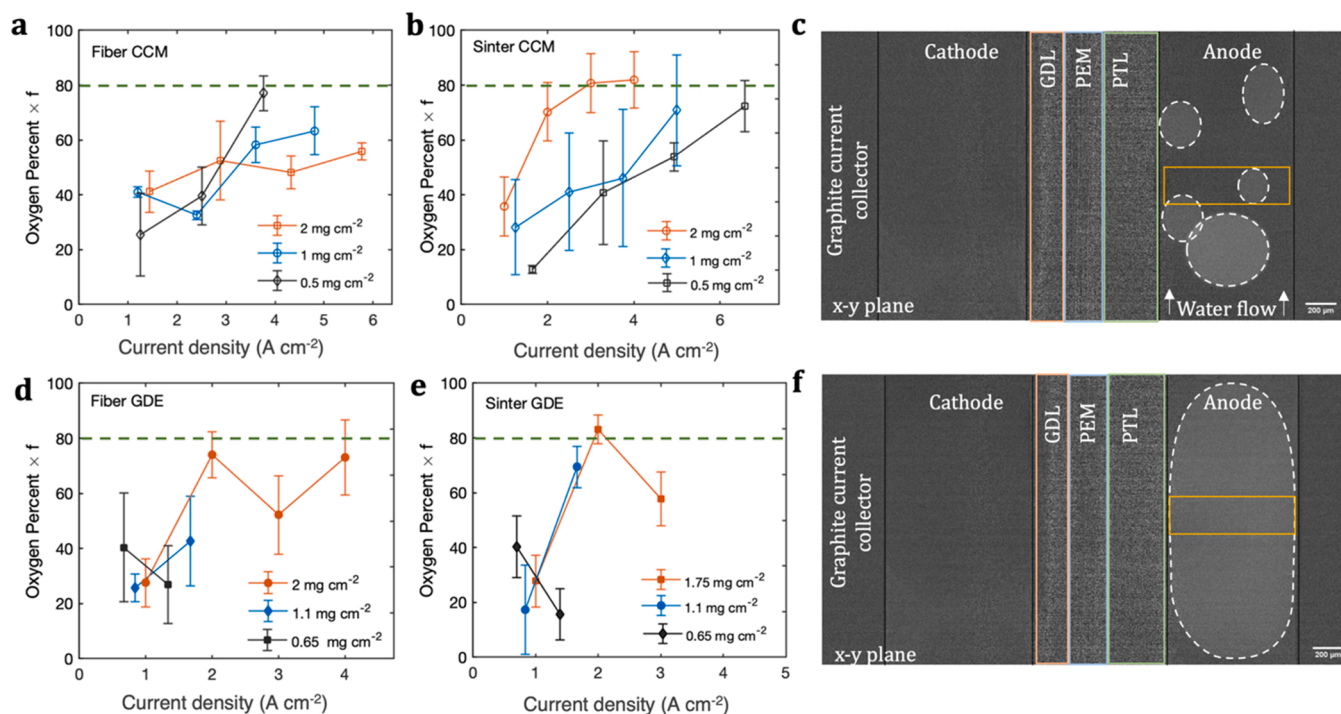
images at different current densities at several locations at the anode channel. Fig. 7 indicates the oxygen content in the channels at various current densities for all samples at constant water flow rate of 3 mlpm. Fig. S18 shows the effect of different water flow rates on the oxygen residence in channel, as well as cell performance. The image processing for extracting oxygen content considers the average grayscale values that pass through the ROI. The correction factor  $f$  quantifies the extent to which the removal of oxygen occurs as discrete bubbles or slugs. A higher  $f$  signifies a higher slug flow regime and vice versa as shown in Fig. 7c and Fig. 7f, respectively. Oxygen content multiplied by  $f$  was measured through x-ray radiography and  $f$  cannot be decoupled from oxygen content. When the channel is fully filled by oxygen then oxygen content times  $f$  will be equal to 1, however, when the channel is filled by water this value will be 0. For CCMs generally oxygen percentage in the channel increased with increase in current density. This is expected, as with more oxygen generated and the same water flow-rate oxygen content in the channel should increase. For fiber CCMs, we observed a slower increase in oxygen percentage in the channel compared to the sinter CCMs, as seen in Fig. 7a and b. Slower increase in oxygen content in the channel suggests that either oxygen accumulates within the PTL, the catalyst layer, or the  $f$  factor is smaller, indicating removal of oxygen as bubbles and not slugs. The last explanation is very likely, as with fiber PTL the fibers are smooth and there is lower number of sites for bubble nucleation compared to sintered PTL. With higher number of nucleation sites, the bubbles coalesce and are removed in the slug form. In case of sintered CCMs, a clear trend was evident, for the same current density a CCM with higher loading show higher content of oxygen in the channel (Fig. 7b). This is indicative that at higher loadings oxygen travels through more pathways within the PTL and then nucleates on more sites after which bubbles coalesce into slugs, showing higher  $f$  factor. For high loadings, the oxygen content plateaus as the current density nears  $4 \text{ A cm}^{-2}$ . As the oxygen content in the channel nears 80%, we observed a sharp increase in the potential since most of the transport pathways were occupied leading to insufficient flow of water to the active sites.

Hence, we can safely assume 80% as the upper oxygen saturation limit in the channels beyond which unstable PEMWE performance at high current densities will occur.

For high loaded GDEs, the oxygen content increased to about 80% and plateaued at  $2 \text{ A cm}^{-2}$ . As the current density increased further to  $3 \text{ A cm}^{-2}$ , there was an apparent drop in the oxygen content as seen in Fig. 7d, e. This may be due to variation in the correction factor  $f$  due to varying flow regimes. The low loaded GDEs also show a drop in oxygen content as current density nears  $2 \text{ A cm}^{-2}$ . During x-ray CT beamtime GDEs were not able to support current densities higher than  $2 \text{ A cm}^{-2}$ , hence the radiography data is missing for higher current densities. Generally, well-functioning PTLs and CCMs or GDEs should show increase in oxygen content in the channel with increase in current density, as shown by Fig. 7b. However, above 80% oxygen content in the channel will result in mass transport limitations.

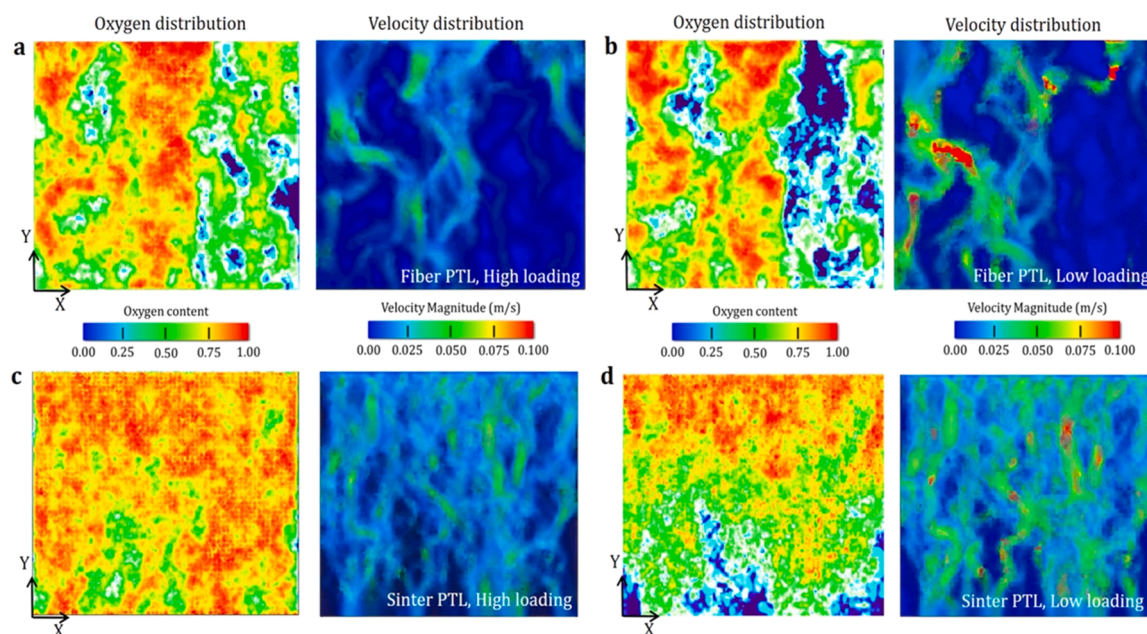
### 3.7. The effect of catalyst loading on the oxygen transport in the porous transport layer

Fig. 8 shows the model prediction and comparison of oxygen content and velocity distributions in the different PTLs with varied catalyst loading. Fig. 8a shows the oxygen content (left) and velocity distribution (right) for the fiber PTL at high catalyst loading. Figs. S20 – S22 show the 3D volume rendering of the oxygen concentration for high, medium, and low loaded fiber PTL, sintered PTL and associated velocity profiles, respectively. The oxygen bubbles were generated at the top of the PTL at the catalyst layer and they transported through the PTL via preferential pathways. The oxygen tended to merge at the PTL mid portion where the higher porosity band is located. The average oxygen velocity in the PTL was about  $0.056 \text{ m s}^{-1}$  for current density of  $1 \text{ A cm}^{-2}$ . At low catalyst loading for fiber PTL, there was lower oxygen content existing in the PTL because oxygen did not take some of the possible transport pathways, as shown in Fig. 8b. This is because of a smaller inlet area for oxygen corresponding to less homogeneous catalyst distribution based on our



**Fig. 7.** Oxygen content in channels as a function of current density for a, b) fiber and sintered CCMs d, e) fiber and sintered GDEs obtained from X-ray radiography c, f) through-plane radiography images of two cells showing the ROI (yellow rectangle) and oxygen bubbles (dotted circles). The oxygen content detected is a function of current density as well as the correction factor  $f$ . The correction factor  $f$  depends on the size of the bubble flowing through the ROI. The magnitude of  $f$  is considered large for a slug flow regime as indicated in f and small for discretized bubble flow as indicated in c.





**Fig. 8.** Modeling prediction of oxygen flow and corresponding velocity profiles in a) High loaded fiber PTL, b) Low loaded fiber PTL, c) high loaded sintered PTL, and d) low loaded sintered PTL. Left of each figure show the volume profiles and right of each figure show the corresponding velocity profiles. The top part of each image is the catalyst layer. The model assumes uniform distribution of catalyst for high loaded samples and non-uniform distribution for low loaded sample. The model was operated at the current density of  $1 \text{ A cm}^{-2}$  with the flow rate of 2 mlpm.

assumptions, which resulted in a low active number of catalytic sites. The average velocity in this case was about  $0.068 \text{ m s}^{-1}$ , which was higher than the high catalyst loading case because of lower number of pathways that oxygen was taking (lower cross-section area that the flux crosses). Importantly, for low loaded sample (Fig. 8b) there were locations where velocity magnitude was as high as  $0.1 \text{ m s}^{-1}$ . It is undesirable to have local high flux locations within the PTL, as if these pathways were to be blocked, significant mass-transport losses are expected.

Fig. 8c and Fig. 8d show oxygen transport through the sintered PTL with the high and low catalyst loading, respectively. At high catalyst loading, oxygen was taking all the possible transport pathways with a high amount of oxygen content within the PTL. Oxygen concentration in sintered PTL was very different than in fiber PTL. This is mainly due to pore sizes of the PTLs. Sintered PTLs have very uniform pore-size distribution with a mean radius of  $8.1 \mu\text{m}$ , as shown in Fig. S16. The cumulative oxygen content in the PTLs is reported in Fig. S23. Oxygen will be transported as a front within the first  $100 \mu\text{m}$ , as shown by Fig. 8c and Fig. S23 for high catalyst loading. After that, the oxygen saturation decreases through the rest of the PTL until it reaches the channel. These results are consistent with experimental findings from De Angelis et al. [58]. Since most of the pores were of the same size there were no preferential pathways for oxygen to take, and there was no higher porosity in the middle of the PTL, as shown for fiber PTLs. There are more pathways for transport existing in this case, which shows a large amount of oxygen content distribution in the PTL. The velocity vectors were very uniform, showing that all the pores within the PTL were utilized for oxygen transport. At low catalyst loading, oxygen front was suppressed, and velocity profile show several bottlenecks with  $0.1 \text{ m s}^{-1}$  maximum velocities. The LBM suggests that preferential transport through the PTL occurred when PSD was non-uniform, such as for fiber PTLs (Fig. S16). The advantage of fiber PTLs is that water delivery can be efficient, as oxygen does not occupy all the pores, however, it can also result in blockage of oxygen transport pathways. For the sintered PTLs very uniform oxygen transport through the PTLs was observed, even for low loaded PTLs, which is desirable.

### 3.8. Durability analysis

The cell durability was probed after steady state electrolyzer operation for 90 h. The cells were allowed to reach a steady state at  $50^\circ\text{C}$  temperature and 30 bar  $\text{H}_2$  pressure before collecting BOL polarization curves. The cells were then held at a constant current density of  $1.8 \text{ A cm}^{-2}$  for 90 h (Fig. S24) at a constant water flow rate on the anode, and the same operating conditions of temperature and pressure. Subsequently, the EOL polarization curves were collected. The testing focused on the influence of interfaces and PTLs on the steady operation, while the other cell components, such as the membrane, current collectors, back pressure etc. were kept constant. The steady-state analysis was conducted as opposed to the established triangle and square wave potential perturbation as accelerated stress tests [59,60] to maintain focus on the effect of electrode configurations on the potential response and establish a baseline in the interface engineering efforts for existing systems.

The measured BOL and EOL polarization curves (Fig. 9a-d) and the corresponding potentials at  $1.5 \text{ A cm}^{-2}$  (Fig. 9e) are shown for all samples. High loaded fiber CCMs show a similar activation potential at low current densities of  $0.1 \text{ A cm}^{-2}$  but show about 100 mV increase in overpotential at  $1.5 \text{ A cm}^{-2}$  at the EOL, as shown in Fig. 9a. However, for low loadings, fiber CCMs showed a substantial 570 mV rise at  $1.5 \text{ A cm}^{-2}$  and over 200 mV rise in activation potential at low current densities at the EOL. As can be seen from Fig. 9b, for high and medium loaded sintered CCMs, the EOL voltage followed approximately a constant 100 mV rise in overpotential until  $2 \text{ A cm}^{-2}$ . For low loaded sintered CCM, the EOL polarization curves showed a 100 mV decrease in overpotential at  $1.5 \text{ A cm}^{-2}$ . Although the BOL polarization curve stood at a substantially higher 800 mV than the high and medium loaded sample, a decrease in overpotential suggests possible conditioning even after 90 h of steady state operation.

## 4. Conclusions

A systematic matrix of twelve PEMWE configurations with two different types of PTLs, two types of electrode configurations namely



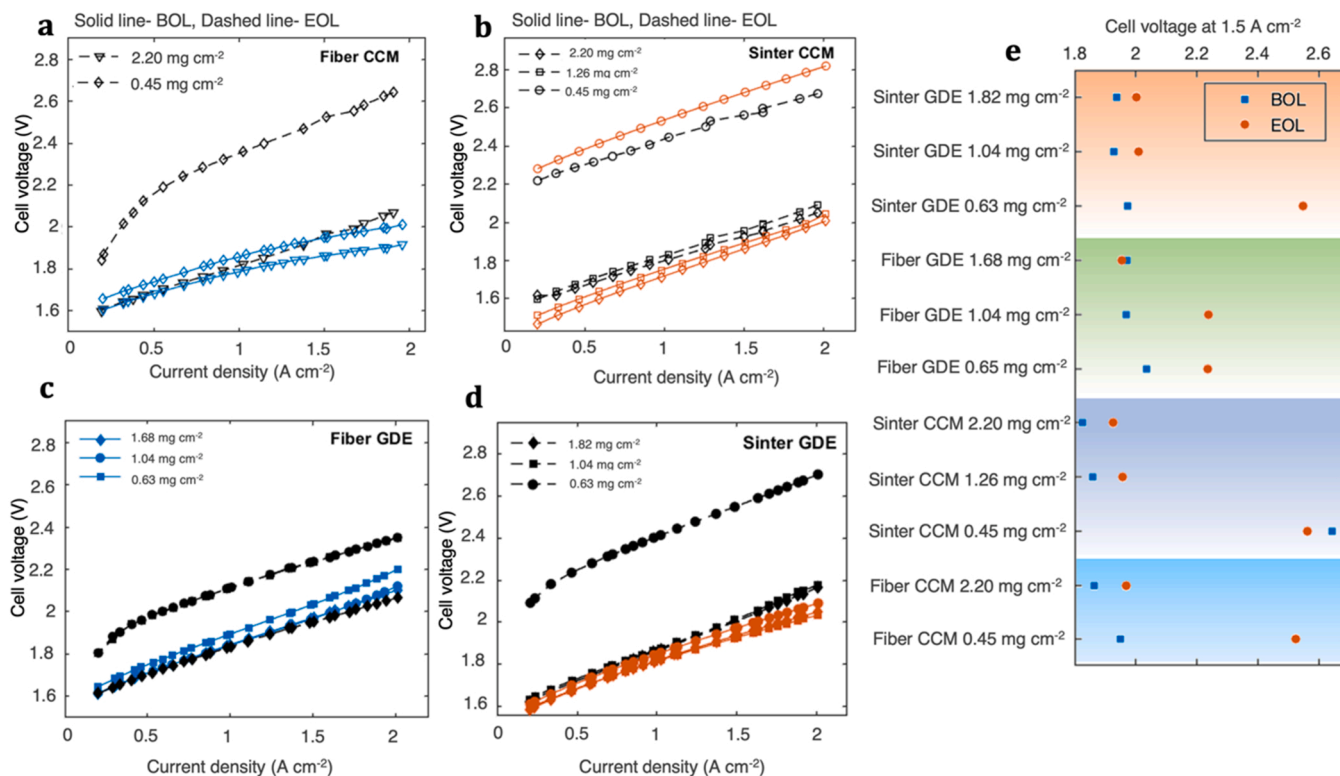


**Fig. 9.** BOL and EOL polarization curves for a, b) fiber and sintered CCMs respectively c, d) fiber and sintered GDEs respectively e) Initial and final potential for all configurations at 1.5 A cm<sup>-2</sup>. The tests were conducted at 50 °C in a 28 cm<sup>2</sup> active area cell. The final polarization curves were obtained after holding each cell at a current density of 1 A cm<sup>-2</sup> for 90 h. The filled symbols represent fiber PTLs, and hollow symbols represent sintered PTLs.

CCM and GDE and three levels of catalyst loadings were characterized using x-ray micro-CT to quantify the interfaces and elucidate their effect on electrochemical performance and gas transport in flow-field channels. Moreover, steady-state durability testing of all the samples was conducted and a Lattice Boltzmann Method model was constructed based on the tomography results to simulate gas transport in the two types of PTLs for varied catalyst loadings. From the tomography images, it was clear that the catalyst agglomeration and clustering increases with loadings for the CCMs and the catalyst conforms to the PTL surface during coating for the GDEs. The calculated TPCA was correlated with the double layer capacities obtained by electrochemical testing. In general, the TPCA increases with increase in catalyst loadings and  $C_{dl}$  scales proportionally. The conjunction of the TPCA along with  $C_{dl}$  gives us a measure of the electrochemically active surface area. The PTL surface morphology plays a vital role in affecting the TPCA. High loaded sintered CCM showed the highest TPCA and concomitantly highest  $C_{dl}$  among all other samples.

The general order of  $C_{dl}$  vs TPCA on the parameter space for CCMs is sintered CCM 0.5 mg cm<sup>-2</sup> < fiber CCM 0.5 mg cm<sup>-2</sup> < fiber CCM 1 mg cm<sup>-2</sup> < sintered CCM 1 mg cm<sup>-2</sup> < fiber CCM 2 mg cm<sup>-2</sup> < sintered CCM 2 mg cm<sup>-2</sup>. This directly relates to the BOL potential measured at 1.5 A cm<sup>-2</sup>, where the cell overpotentials follow the same exact trend. Similarly, the general order of  $C_{dl}$  vs TPCA on the parameter space for GDEs is sintered GDE 0.65 mg cm<sup>-2</sup> < fiber GDE 0.65 mg cm<sup>-2</sup> < fiber GDE 1.1 mg cm<sup>-2</sup> < sintered GDE 1.1 mg cm<sup>-2</sup> < fiber GDE 1.75 mg cm<sup>-2</sup> < sintered GDE 1.75 mg cm<sup>-2</sup>. This trend relates directly with the measured improvement in overpotential until medium loadings, but high loaded fiber GDE shows a ~ 30 mV rise than sintered GDE. The discrepancies associated with such performance loss especially in GDEs is attributed to influence of undesirable overpotentials that affect the kinetics as shown by the Tafel analysis. The Tafel analysis shows that on average GDE configurations had higher Tafel slopes compared to CCM configurations, indicating that there are some other non-kinetic losses

are present. Low loaded GDEs show the most performance loss after steady state current density holds possibly due to mechanical degradation of the catalyst. The investigation of oxygen content in the channels sheds light on the mass transport overpotentials. We determine 80% oxygen in the channel to be the maximum to avoid water depletion in the catalyst layer. CCM configurations showed increase in oxygen content in the channel with increase in current density, as at higher current density more oxygen is produced and removed in the channel. The 3-D modeling suggests that for low-loaded catalyst layers the pathways for oxygen transport through the PTLs are limited, as oxygen is transported through a few preferential pathways. Fiber PTL has larger pores and more inhomogeneous pore size distribution leading to preferential oxygen transport pathways even at high catalyst loading. Sintered PTLs have more uniform and smaller pores, resulting in more uniform oxygen distribution in the PTL.

These findings add in-depth experimental and modeling insight into the nature of the PTL-catalyst layer interface and contribute to the understanding of impact of PTL bulk properties on gas and water transport. From these findings the following design guidelines for PEMWE can be proposed:

- o Sintered CCMs with 44.7% porosity can be used to obtain a high triple phase contact area between the catalyst layer and PTL and better gas removal at loadings above 0.5 mg cm<sup>-2</sup>.
- o Uniform gas removal through the PTL results in the slug flow regime and the optimal oxygen saturation in the channels should be 80% or below to ensure stable performance at high current densities.
- o The catalyst utilization is affected by the nature of the catalyst layer and morphology of the PTL, since GDEs can be limited by proton transport and CCMs can be limited by electron transport. To have highly active TPCA the PTL surface can be tailored to have larger area of deposited catalyst contacting the membrane.

- o For commercial electrolyzers with immediate demand, we recommend using sintered CCMs with 0.5–1 mg cm<sup>-2</sup> loadings of unsupported IrOx for reasonable overpotentials at high current densities and since any higher loading does not result in significant durability or overpotential improvement. Significant research effort is needed in catalyst ink optimization and coating to reach lower loadings but maintain durability.

### CRedit authorship contribution statement

**Devashish Kulkarni:** Conceptualization, Methodology, Investigation, Resources, Data curation, Writing – original draft, Visualization. **Iryna Zenyuk:** Conceptualization, Methodology, Investigation, Resources, Data curation, Writing – original draft, Visualization. **Alex Huynh:** Conceptualization, Methodology, Investigation, Resources, Data curation, Writing – original draft, Visualization. **Pongsarun Satjaritanun:** Conceptualization, Methodology, Investigation, Resources, Data curation, Writing – original draft, Visualization. **Maeve O'Brien:** Conceptualization, Methodology, Investigation, Resources, Data curation, Writing – original draft, Visualization. **Iryna Zenyuk:** Funding acquisition, supervision, Writing – review & editing, Resources. **Christopher Capuano:** Funding acquisition, supervision, Writing – review & editing, Resources. **Kathrine E Ayers:** Funding acquisition, supervision, Writing – review & editing, Resources. **Dilworth Parkinson:** Investigation, Formal analysis. **Francesco DeCarlo:** Investigation, Formal analysis. **Pavel Shevchenko:** Investigation, Formal analysis. **Nemanja Danilovic:** Writing – review & editing. **Sirivatch Shimpalee:** Writing – review & editing.

### Declaration of Competing Interest

The authors declare that they have no known competing financial interests or personal relationships that could have appeared to influence the work reported in this paper.

### Acknowledgements

All of the authors would like to acknowledge funding from the HydroGEN Advanced Water Splitting Materials Consortium, established as part of the Energy Materials Network under the U.S. Department of Energy, Office of Energy Efficiency and Renewable Energy, Fuel Cell Technologies Office and program managers David Peterson and Katie Randolph. This work was supported by U.S. Department of Energy EERE award number EE0008081. This research used beamline 2-BM-A of the Advanced Photon Source; a U.S. Department of Energy (DOE) Office of Science User Facility operated for the DOE Office of Science by Argonne National Laboratory under Contract No. DE-AC02-06CH11357. This research used beamline 8.3.2 of the Advanced Light Source, which is a DOE Office of Science User Facility under contract no. DE-AC02-05CH11231. We acknowledge Emily Leonard for conducting the water flow rate and associated cell performance measurements. The authors would like to acknowledge Dassault Systèmes Simulia S.L.U. for providing the XFlow software. Dragonfly 2020.2 is a software developed by Object Research Systems (ORS) Inc, Montreal, Canada and is available at <http://www.theobjects.com/dragonfly>.

### Declaration of competing interests

The authors declare that they have no known competing financial interests or personal relationships that could have appeared to influence the work reported in this work.

### Appendix A. Supporting information

Supplementary data associated with this article can be found in the online version at [doi:10.1016/j.apcatb.2022.121213](https://doi.org/10.1016/j.apcatb.2022.121213).

### References

- [1] S. Ould Amrouche, D. Rekioua, T. Rekioua, S. Bacha, Overview of energy storage in renewable energy systems, *Int. J. Hydrog. Energy* 41 (45) (2016) 20914–20927, <https://doi.org/10.1016/j.ijhydene.2016.06.243>.
- [2] A. Evans, V. Strezov, T.J. Evans, Assessment of utility energy storage options for increased renewable energy penetration, *Renew. Sustain. Energy Rev.* vol. 16 (6) (2012) 4141–4147, <https://doi.org/10.1016/j.rser.2012.03.048>.
- [3] A. Ozarslan, Large-scale hydrogen energy storage in salt caverns, *Int. J. Hydrog. Energy* 37 (19) (2012) 14265–14277, <https://doi.org/10.1016/j.ijhydene.2012.07.111>.
- [4] A. Saeedmanesh, M.A. Mac Kinnon, J. Brouwer, Hydrogen is essential for sustainability, *Curr. Opin. Electrochem.* vol. 12 (2018) 166–181, <https://doi.org/10.1016/j.coelec.2018.11.009>.
- [5] M. Kayfeci, A. Kecebas, Hydrogen storage, *Sol. Hydrog. Prod. Process. Syst. Technol.* (2019) 85–110, <https://doi.org/10.1016/B978-0-12-814853-2.00004-7>.
- [6] G.H. Rau, H.D. Willauer, Z.J. Ren, The global potential for converting renewable electricity to negative-CO<sub>2</sub>-emissions hydrogen, *Nat. Clim. Chang.* vol. 8 (7) (2018) 621–625, <https://doi.org/10.1038/s41558-018-0203-0>.
- [7] M. Ali, J. Ekström, M. Lehtonen, Sizing hydrogen energy storage in consideration of demand response in highly renewable generation power systems, *Energies* 11 (5) (2018), <https://doi.org/10.3390/en11051113>.
- [8] K. Ayers, N. Danilovic, R. Ouimet, M. Carmo, B. Pivovar, M. Bornstein, Perspectives on low-temperature electrolysis and potential for renewable hydrogen at scale, *Annu. Rev. Chem. Biomol. Eng.* 10 (1) (2019) 219–239, <https://doi.org/10.1146/annurev-chembioeng-060718-030241>.
- [9] P. Patel, K. Ayers, *Electro Hydrog. Prod.* 44 (9) (2019).
- [10] B. Pivovar, N. Rustagi, S. Satyapal, Hydrogen at scale (H2@Scale) key to a clean, economic, and sustainable energy system, *Electrochem. Soc. Interface* vol. 27 (2018) 47–52.
- [11] T. Van de Graaf, I. Overland, D. Scholten, K. Westphal, The new oil? The geopolitics and international governance of hydrogen, *Energy Res. Soc. Sci.* 70 (2020), 101667, <https://doi.org/10.1016/j.erss.2020.101667>.
- [12] DOE, Fuel cell technologies program multi-year research. Development, and Demonstration Plan, US Department of Energy Washington, DC, 2007.
- [13] T. Reier, H.N. Nong, D. Teschner, R. Schlögl, P. Strasser, Electrocatalytic oxygen evolution reaction in acidic environments – reaction mechanisms and catalysts, *Adv. Energy Mater.* 7 (1) (2017), <https://doi.org/10.1002/aenm.201601275>.
- [14] M. Carmo, D.L. Fritz, J. Mergel, D. Stolten, A comprehensive review on PEM water electrolysis, *Int. J. Hydrog. Energy* vol. 38 (12) (2013) 4901–4934, <https://doi.org/10.1016/j.ijhydene.2013.01.151>.
- [15] K.E. Ayers, et al., Pathways to ultra-low platinum group metal catalyst loading in proton exchange membrane electrolyzers, *Catal. Today* 262 (2016) 121–132, <https://doi.org/10.1016/j.cattod.2015.10.019>.
- [16] Z. Taie, et al., Pathway to complete energy sector decarbonization with available iridium resources using ultralow loaded water electrolyzers, *ACS Appl. Mater. Interfaces* (2020), <https://doi.org/10.1021/acsami.0c15687>.
- [17] U. Babic, M. Suermann, F.N. Büchi, L. Gubler, T.J. Schmidt, Critical review—identifying critical gaps for polymer electrolyte water electrolysis development, *J. Electrochem. Soc.* vol. 164 (4) (2017) F387–F399, <https://doi.org/10.1149/2.1441704jes>.
- [18] M. Bernt, Analysis of Voltage Losses and Degradation Phenomena in PEM Water Electrolyzers Maximilian Philipp Bernt, 2019.
- [19] S. Siracusano, V. Baglio, N. Van Dijk, L. Merlo, A.S. Aricò, Enhanced performance and durability of low catalyst loading PEM water electrolyser based on a short-side chain perfluorosulfonic ionomer, *Appl. Energy* 192 (2017) 477–489, <https://doi.org/10.1016/j.apenergy.2016.09.011>.
- [20] B.S. Lee, et al., Polarization characteristics of a low catalyst loading PEM water electrolyzer operating at elevated temperature, *J. Power Sources* vol. 309 (2016) 127–134, <https://doi.org/10.1016/j.jpowsour.2015.12.139>.
- [21] L. Ma, S. Sui, Y. Zhai, Investigations on high performance proton exchange membrane water electrolyzer, *Int. J. Hydrog. Energy* 34 (2) (2009) 678–684, <https://doi.org/10.1016/j.ijhydene.2008.11.022>.
- [22] P. Mazúr, J. Polonský, M. Paidar, K. Bouzek, Non-conductive TiO<sub>2</sub> as the anode catalyst support for PEM water electrolysis, *Int. J. Hydrog. Energy* 37 (17) (2012) 12081–12088, <https://doi.org/10.1016/j.ijhydene.2012.05.129>.
- [23] K.A. Lewinski, D. van der Vliet, S.M. Luopa, NSTF advances for PEM Electrolysis - the effect of alloying on activity of NSTF electrolyzer catalysts and performance of NSTF based PEM electrolyzers, *ECS Trans.* 69 (17) (2015) 893–917, <https://doi.org/10.1149/06917.0893ecst>.
- [24] L. Du, L. Xing, G. Zhang, M. Dubois, S. Sun, Strategies for engineering high-performance PGM-free catalysts toward oxygen reduction and evolution reactions, *Small Methods* 4 (6) (2020) 1–28, <https://doi.org/10.1002/smt.202000016>.
- [25] M. Bernt, A. Siebel, H.A. Gasteiger, Analysis of voltage losses in PEM water electrolyzers with low platinum group metal loadings, *J. Electrochem. Soc.* vol. 165 (5) (2018) F305–F314, <https://doi.org/10.1149/2.0641805jes>.
- [26] A. Badgett, M. Ruth, B. Pivovar, *Economic Considerations for Hydrogen Production with a Focus on Polymer Electrolyte Membrane Electrolysis*, Elsevier B.V., 2022.
- [27] T. Schuler, R. De Bruycker, T.J. Schmidt, F.N. Büchi, Polymer electrolyte water electrolysis: correlating porous transport layer structural properties and performance: Part i. tomographic analysis of morphology and topology, *J. Electrochem. Soc.* 166 (4) (2019) F270–F281, <https://doi.org/10.1149/2.0561904jes>.
- [28] T. Schuler, T.J. Schmidt, F.N. Büchi, Polymer electrolyte water electrolysis: correlating performance and porous transport layer structure: part ii.

- electrochemical performance analysis, *J. Electrochem. Soc.* 166 (10) (2019) F555–F565, <https://doi.org/10.1149/2.1241908jes>.
- [29] J. Lopata, Z. Kang, J. Young, G. Bender, J.W. Weidner, S. Shimpalee, Effects of the transport/catalyst layer interface and catalyst loading on mass and charge transport phenomena in polymer electrolyte membrane water electrolysis devices, *J. Electrochem. Soc.* vol. 167 (6) (2020), 064507, <https://doi.org/10.1149/1945-7111/ab7f87>.
- [30] E. Leonard, et al., Interfacial analysis of a PEM electrolyzer using X-ray computed tomography, *Sustain. Energy Fuels* (2020) 921–931, <https://doi.org/10.1039/c9se00364a>.
- [31] X. Peng, et al., Insights into interfacial and bulk transport phenomena affecting proton exchange membrane water electrolyzer performance at ultra-low iridium loadings, *Adv. Sci.* 8 (21) (2021) 1–9, <https://doi.org/10.1002/adv.202102950>.
- [32] J.K. Lee, et al., Accelerating bubble detachment in porous transport layers with patterned through pores, *ACS Appl. Energy Mater.* (2020), <https://doi.org/10.1021/acsaem.0c01239>.
- [33] M.A. Hoeh, et al., In-operando neutron radiography studies of polymer electrolyte membrane water electrolyzers, *ECS Trans.* 69 (17) (2015) 1135–1140, <https://doi.org/10.1149/06917.1135ecst>.
- [34] O.F. Selamet, U. Pasaogullari, D. Spornjak, D.S. Hussey, D.L. Jacobson, M.D. Mat, Two-phase flow in a proton exchange membrane electrolyzer visualized in situ by simultaneous neutron radiography and optical imaging, *Int. J. Hydrog. Energy* 38 (14) (2013) 5823–5835, <https://doi.org/10.1016/j.ijhydene.2013.02.087>.
- [35] P. Satjaritanun, et al., iScience observation of preferential pathways for oxygen removal through porous transport layers of polymer electrolyte water electrolyzers observation of preferential pathways for oxygen removal through porous transport layers of polymer electrolyte water, *ISCIENCE* 23 (12) (2020), 101783, <https://doi.org/10.1016/j.isci.2020.101783>.
- [36] D. Kulkarni, S.J. Normile, L.G. Connolly, I.V. Zenyuk, Development of low temperature fuel cell holders for Operando x-ray micro and nano computed tomography to visualize water distribution, *J. Phys. Energy* 2 (4) (2020), 044005, <https://doi.org/10.1088/2515-7655/abb783>.
- [37] D. Gürsoy, F. De Carlo, X. Xiao, C. Jacobsen, TomoPy: a framework for the analysis of synchrotron-tomographic data, *J. Synchrotron Radiat.* 21 (5) (2014) 1188–1193, <https://doi.org/10.1107/S1600577514013939>.
- [38] A. Serov, et al., Nano-structured platinum group metal-free catalysts and their integration in fuel cell electrode architectures, *Appl. Catal. B Environ.* 237 (2017) 1139–1147, <https://doi.org/10.1016/j.apcatb.2017.08.067>.
- [39] A.D. Shum, D.Y. Parkinson, X. Xiao, A.Z. Weber, O.S. Burheim, I.V. Zenyuk, Investigating phase-change-induced flow in gas diffusion layers in fuel cells with X-ray computed tomography, *Electrochim. Acta* 256 (2017) 279–290, <https://doi.org/10.1016/j.electacta.2017.10.012>.
- [40] P. Satjaritanun, F.C. Cetinbas, S. Hirano, I.V. Zenyuk, R.K. Ahluwalia, S. Shimpalee, Hybrid lattice boltzmann agglomeration method for modeling transport phenomena in polymer electrolyte membrane fuel cells, *J. Electrochem. Soc.* vol. 168 (4) (2021), 044508, <https://doi.org/10.1149/1945-7111/abf217>.
- [41] M. Sepe, P. Satjaritanun, S. Hirano, I.V. Zenyuk, N. Tippayawong, S. Shimpalee, Investigating liquid water transport in different pore structure of gas diffusion layers for PEMFC using lattice boltzmann method, *J. Electrochem. Soc.* 167 (10) (2020), 104516, <https://doi.org/10.1149/1945-7111/ab9d13>.
- [42] P. Satjaritanun, et al., Numerical predicting of liquid water transport inside gas diffusion layer for PEMFC Using lattice Boltzmann method, *ECS Trans.* 80 (8) (2017) 187–195, <https://doi.org/10.1149/08008.0187ecst>.
- [43] S.M. Alia, K.S. Reeves, J.S. Baxter, D.A. Cullen, The impact of ink and spray variables on catalyst layer properties, electrolyzer performance, and electrolyzer durability, *J. Electrochem. Soc.* 167 (14) (2020), 144512, <https://doi.org/10.1149/1945-7111/abc746>.
- [44] J. Mo, et al., Discovery of true electrochemical reactions for ultrahigh catalyst mass activity in water splitting, *Sci. Adv.* 2 (11) (2016), <https://doi.org/10.1126/sciadv.1600690>.
- [45] T. Schuler, T. Kimura, T.J. Schmidt, F.N. Büchi, Towards a generic understanding of oxygen evolution reaction kinetics in polymer electrolyte water electrolysis, *Energy Environ. Sci.* 13 (7) (2020) 2153–2166, <https://doi.org/10.1039/d0ee00673d>.
- [46] T. Schuler, et al., Hierarchically structured porous transport layers for polymer electrolyte water electrolysis, *Adv. Energy Mater.* 1903216 (2019) 1903216–1903228, <https://doi.org/10.1002/aenm.201903216>.
- [47] N.M. Marković, B.N. Grgur, P.N. Ross, Temperature-dependent hydrogen electrochemistry on platinum low-index single-crystal surfaces in acid solutions, *J. Phys. Chem. B* 101 (27) (1997) 5405–5413, <https://doi.org/10.1021/jp970930d>.
- [48] G. Jerkiewicz, Electrochemical hydrogen adsorption and absorption. Part 1: underpotential deposition of hydrogen, *Electrocatalysis* 1 (4) (2010) 179–199, <https://doi.org/10.1007/s12678-010-0022-1>.
- [49] S.M. Alia, K.E. Hurst, S.S. Kocha, B.S. Pivovar, Mercury underpotential deposition to determine iridium and iridium oxide electrochemical surface areas, *J. Electrochem. Soc.* 163 (11) (2016) F3051–F3056, <https://doi.org/10.1149/2.0071611jes>.
- [50] S. Zhao, et al., Calculating the Electrochemically active surface area of iridium oxide in operating proton exchange membrane electrolyzers, *J. Electrochem. Soc.* 162 (12) (2015) F1292–F1298, <https://doi.org/10.1149/2.0211512jes>.
- [51] M. Suermann, T.J. Schmidt, F.N. Büchi, Cell performance determining parameters in high pressure water electrolysis, *Electrochim. Acta* vol. 211 (2016) 989–997, <https://doi.org/10.1016/j.electacta.2016.06.120>.
- [52] M. Kroschel, A. Bonakdarpour, J.T.H. Kwan, P. Strasser, D.P. Wilkinson, Analysis of oxygen evolving catalyst coated membranes with different current collectors using a new modified rotating disk electrode technique, *Electrochim. Acta* 317 (2019) 722–736, <https://doi.org/10.1016/j.electacta.2019.05.011>.
- [53] S. Siracusano, et al., Electrochemical characterization of single cell and short stack PEM electrolyzers based on a nanosized IrO<sub>2</sub> anode electrocatalyst, *Int. J. Hydrog. Energy* 35 (11) (2010) 5558–5568, <https://doi.org/10.1016/j.ijhydene.2010.03.102>.
- [54] T. Shinagawa, A.T. Garcia-Esparza, K. Takanabe, Insight on Tafel slopes from a microkinetic analysis of aqueous electrocatalysis for energy conversion, *Sci. Rep.* (2015) 1–21, <https://doi.org/10.1038/srep13801>.
- [55] H<sub>2</sub>-transport limitations in the hydrogen electrode in PEM water electrolysis, *ECS Meet. Abstr.* (2017), <https://doi.org/10.1149/ma2017-01/31/1513>.
- [56] R. Iwata, et al., Bubble growth and departure modes on wettable/non-wettable porous foams in alkaline water splitting, *Joule* 5 (4) (2021) 887–900, <https://doi.org/10.1016/j.joule.2021.02.015>.
- [57] T. Kadyk, D. Bruce, M. Eikerling, How to enhance gas removal from porous electrodes? *Sci. Rep.* 6 (2016) 1–14, <https://doi.org/10.1038/srep38780>.
- [58] S. De Angelis, T. Schuler, M.A. Charalambous, F. Marone, T.J. Schmidt, F.N. Büchi, Unraveling two-phase transport in porous transport layer materials for polymer electrolyte water electrolysis, *J. Mater. Chem. A* 9 (38) (2021) 22102–22113, <https://doi.org/10.1039/d1ta03379d>.
- [59] S.M. Alia, S. Stariha, R.L. Borup, Electrolyzer durability at low catalyst loading and with dynamic operation, *J. Electrochem. Soc.* 166 (15) (2019) F1164–F1172, <https://doi.org/10.1149/2.0231915jes>.
- [60] P. Aßmann, A.S. Gago, P. Gazdzicki, K.A. Friedrich, M. Wark, Toward developing accelerated stress tests for proton exchange membrane electrolyzers, *Curr. Opin. Electrochem.* (2020) 225–233, <https://doi.org/10.1016/j.coelec.2020.02.024>.